



# Robust monolithic versus distributed control/structure co-optimization of flexible space systems in presence of parametric uncertainties

Francesco Sanfedino<sup>1</sup> · Daniel Alazard<sup>1</sup> · Andy Kiley<sup>2</sup> · Mark Watt<sup>2</sup> · Pedro Simplicio<sup>3</sup> · Finn Ankersen<sup>3</sup>

Received: 30 May 2023 / Revised: 4 September 2023 / Accepted: 30 October 2023 / Published online: 27 November 2023  
© The Author(s), under exclusive licence to Springer-Verlag GmbH Germany, part of Springer Nature 2023

## Abstract

This paper presents an end-to-end framework for robust structure/control optimization of an industrial benchmark. When dealing with space structures, a reduction of the spacecraft mass is paramount to minimize the mission cost and maximize the propellant availability. However, a lighter design comes with a bigger structural flexibility and the resulting impact on control performance. Two optimization architectures (*distributed* and *monolithic*) are proposed in order to face this issue. In particular the Linear Fractional Transformation (LFT) framework is exploited to formally set the two optimization problems by including parametric uncertainties. Large sets of uncertainties have to be indeed taken into account in spacecraft control design due to the impossibility to completely validate structural models in micro-gravity conditions with on-ground experiments and to the evolution of spacecraft dynamics during the mission (structure degradation and fuel consumption). In particular the Two-Input Two-Output Port (TITOP) multi-body approach is used to build the flexible dynamics in a minimal LFT form. The two proposed optimization algorithms are detailed and their performance are compared on an ESA future exploration mission, the ENVISION benchmark. With both approaches, an important reduction of the mass is obtained by coping with the mission's control performance/stability requirements and a large set of uncertainties.

**Keywords** Robust optimization · Structure/control co-design · *distributed* Optimization · *monolithic* Optimization · Robust control · Parametric uncertainty

---

Responsible Editor: Xiaoping Du.

✉ Francesco Sanfedino  
francesco.sanfedino@isae.fr

Daniel Alazard  
daniel.alazard@isae.fr

Andy Kiley  
andy.kiley@airbus.com

Mark Watt  
mark.watt@airbus.com

Pedro Simplicio  
pedro.simplicio@ext.esa.int

Finn Ankersen  
finn.ankersen@ieee.org

<sup>1</sup> ISAE-SUPAERO, Université de Toulouse, 10 Av. E. Belin, 31055 Toulouse, France

<sup>2</sup> Airbus DS UK, Gunnels Wood Rd, Stevenage SG1 2AS, UK

<sup>3</sup> ESA-ESTEC, Keplerlaan 1, 2201 AZ Noordwijk, The Netherlands

## 1 Introduction

The widespread approach for multi-disciplinary optimization (MDO) problems adopted in the space industry generally follows a sequential logic by neglecting the interconnection among different disciplines. However, since the optimization objectives in the different fields are often conflicting, this methodology can fail to find global optimal solutions. By restricting the analysis to just structure and control fields, the common hierarchy is to preliminarily define the structure by optimizing the physical design parameters and then leave the floor to the control optimization. This process can be iterated several times before a converging solution is found and control performance is met. Especially for large flexible structures, the minimization of the structural mass corresponds in fact to an increase in spacecraft flexibility, by bringing natural modes to lower frequencies where the interaction with the Attitude and Orbit Control System (AOCS) can be critical, especially in the presence of system uncertainties (Falcoz et al. 2013). Modern MDO techniques

nowadays represents a tool to enhance the optimization task by integrating in a unique process all the objectives and constraints coming from each field. Two kinds of architectures can be distinguished in the MDO framework: *monolithic* and *distributed* (Martins and Lambe 2013). In a *monolithic* approach, a single optimization problem is solved, while in a *distributed* architecture the same problem is partitioned into multiple subproblems containing smaller subsets of the variables and constraints. *monolithic* architectures have been proven to be more efficient (Fathy et al. 2001; Reyer et al. 2001), than classical sequential strategies (Chen and Cheng 2006; Li et al. 2001), especially when bidirectional coupling exists between the two sub-problems (control and structure), for instance, when each of the two objectives depends on some common variables and parameters of each sub-problem (Frischknecht et al. 2011).

In literature, several examples are found where control/structure co-design is implemented in a *monolithic* architecture. Zhao et al. (2009) presented a control-structural design optimization for vibration of piezoelectric intelligent truss structures. Allison et al. (2014) extended the direct transcription method, which transforms infinite-dimensional control design problems into finite-dimensional nonlinear programming problems, for co-design using a new automotive active suspension design example. Maraniello and Palacios (2016) presented an optimal vibration control and co-design strategy for very flexible actuated structures. A standard quasi-Newton method, the Sequential Least Squares Programming (SLSQP) optimization algorithm has been used to solve both the nonlinear optimal control problem and the co-design optimization. The implementation is *monolithic* and uses finite differences for the gradient evaluation. Feng et al. (2014) presented a multi-objective design for flexible spacecraft using a multiobjective evolutionary algorithm based on decomposition (MOEA/D) to reduce the total mass and optimize the control performance of a flexible spacecraft. In Alavi et al. (2021) a Variable Neighborhood Search (VNS) metaheuristic method is developed to both minimize the structural mass and controlled system energy of a seismic civil structure. In He et al. (2023) Genetic Algorithm is used to optimize a passive-active-combined suspension design. However, in all these works the uncertainties of the system are not taken into account.

As suggested in the conclusions of Herber and Allison (2018), where different *monolithic* and *distributed* co-design problems are examined, an important contribution to this research field would be in the inclusion of uncertainties into the MDO process. This inclusion would increase the use of MDO in real engineering problems. In this direction, Azad and Herber (2023) recently published an overview on different uncertain control co-design (UCCD) problem formulations. In this paper they recall the principal theories (stochastic programming, robust optimization and fuzzy pro-

gramming) in which a UCCD formulation is adopted “to meet the ever-increasing demands on performance, robustness, and reliability of real-world dynamic systems”.

The development in last decade of structured  $\mathcal{H}_\infty$  control synthesis (Gahinet and Apkarian 2011) opened the possibility to robust optimal co-design of structured controllers and tunable physical parameters. Linear Fractional Transformation (LFT) formalism allows in fact to embed in the dynamic model tunable physical parameters treated as parametric uncertainties, by interconnection of a known fixed dynamics put in a linear time-invariant (LTI) plant and a perturbation matrix containing all uncertain and varying parameters. The reader is invited to refer to Zhou and Doyle (1998) for an extended overview on LFT formalism and robust control theory. In addition, thanks to these techniques, particular properties can be imposed to the controller, as internal stability or performance respecting a frequency template, in the face of all the parametric uncertainties of the plant. This point is particularly important for aerospace applications where requirements are generally highly demanding and structural uncertainty, coming for example from an imperfect manufacturing or assembling, cannot be neglected. Alazard et al. (2013) demonstrated how this multi-model methodology implemented in  $\mathcal{H}_\infty$  framework can be enlarged to include integrated design between certain tunable parameters of the controlled system and the stabilized structured controller. This approach has been used by Perez et al. (2015) to optimize the structure of a deployable boom from TARANIS microsatellite, while meeting some control requirements.

There exists as well in literature a large class of problems where coupling between structure and control is considered unidirectional (Frischknecht et al. 2011). This means that the objective function  $J_s(\mathbf{y}_s)$  of the structural sub-problem depends only on the structural design parameters  $\mathbf{y}_s$  while the control criterion  $J_c(\mathbf{y}_s, \mathbf{y}_c)$  depends on both structural ( $\mathbf{y}_s$ ) and control ( $\mathbf{y}_c$ ) design parameters, so that the system design objective becomes (Frischknecht et al. 2011):

$$J = w_s J_s(\mathbf{y}_s) + w_c J_c(\mathbf{y}_s, \mathbf{y}_c), \quad (1)$$

where  $w_s$  and  $w_c$  are ponderation weights. A partition of the structure and controller design variables is desirable for practical implementation when the impact of the controller variables on the structural objective is relatively small or computational means are not available to treat simultaneously control and structure variables in the objective function (Frischknecht et al. 2011). A strategy in the latter case suggested by Fathy et al. (2001) and Reyer et al. (2001) is to solve the system-level problem as a nested optimization one, where the system solution is found with respect to  $\mathbf{y}_s$ , with the optimal  $\mathbf{y}_c$  computed as function of  $\mathbf{y}_s$  by solving the inner optimal controller problem first. This nested problem formulation is distinguished from the simultaneous one in

Eq. (1):

$$J^n = w_s J_s(\mathbf{y}_s) + w_c J_c^n(\mathbf{y}_c^*(\mathbf{y}_s)) \quad (2)$$

For this kind of problem, a *distributed* optimization architecture is then more appropriate. There are several works in the literature, where nested optimization is used. Chilan et al. (2017) proposed a strain-actuated solar array concept that enables attitude slewing maneuvers and precision pointing stares for image acquisition, whilst simultaneously suppressing structural vibrations. Zheng et al. (2021) proposed a two layers integrated design optimization of actuator layout and structural ply parameters for the dynamic shape control of piezoelectric laminated curved shell structures.

Two other examples in literature of *distributed* control/structure optimization were provided by the BIOMASS test case (Falcoz et al. 2013; Toglia et al. 2013). In both works, a Genetic Algorithm was used to solve the global optimization problem and robust control techniques were applied for the nested control optimization problem. In the first work, limitations were encountered in the robust synthesis by considering the set of parametric uncertainties and an approximated dynamical uncertainty was instead used for the control synthesis and analysis. A conservative design is generally issued from this procedure and a small reduction of the spacecraft mass was finally obtained. Similar performance is obtained in Toglia et al. (2013), where the controller synthesis does not take into account uncertainties and a formal  $\mu$ -analysis (Zhou and Doyle 1998) is run at each nested iteration in order to validate its robustness. The inconvenience in this approach is twofold: the computational time to run a  $\mu$ -analysis is high, especially in the presence of highly repeated parametric uncertainties (no information on the time performance is provided in the article); not considering uncertainties directly in the controller synthesis can invalidate a large number of controllers.

The present study proposes a comparative study of a robust *monolithic* and *distributed* optimization architectures on an industrial benchmark, the ENVISION spacecraft. In particular, the problem formulation in the multi-body Two-Input Two-Output Ports (TITOP) modeling approach introduced by Alazard et al. (2015) allows the authors to easily define an MDO problem by including all possible system uncertainties from the very beginning of the spacecraft design. In this way, not only is a structure/control co-design possible, but system performance is robustly guaranteed. The novelty of the proposed approach with respect to previous works consists in fully exploiting the potentialities offered by the modern structured robust control synthesis (Apkarian et al. 2007) and the LFT formulation offered by the TITOP approach to deal with a huge number of parametric uncertainties and provide two optimization processes to cope with benchmarks of industrial complexity. The use of robust con-

trol synthesis, not relying on  $\mu$ -based algorithm as in Falcoz et al. (2013), furthermore allows the authors to overcome the limitation imposed by the number (and occurrences) of the uncertain parameters on the computational time and speed up the control synthesis. A formal controller validation is then run only ones at the end of the optimization process. A further contribution of this paper with respect to the the state-of-the-art consists in providing a general LFT formulation to define both a *monolithic* and *distributed* co-optimization problem and compare them on the same industrial benchmark.

The final aim of this paper is, in fact, to contribute to the evolution of industrial practice in robust control/structure co-design, by proposing a unified and generic approach based on a well-posed modeling problem that integrates both design parameters and parametric uncertainties in a unique representation. The advantage offered by this framework is twofold: to shortcut the unnecessary iterations among different fields of expertise and to speed up the validation and verification process by directly producing a robust preliminary design.

The workflow generally followed in the industry can be summarized as follows:: the optimization of structures and control laws is separately done by two different entities which rarely interact by exchanging information in the same nomenclature conventions. Structural models provided by the structure department to the AOCS team are generally very preliminary and an important uncertainty margin has to be taken into account in the control synthesis in order to cover possible evolution of the structural design till its final version. Rarely the optimized design of the structure architecture is updated to reinitialize the control synthesis and analysis process for cost/time reasons. This brings then to conservative control designs that could result in sub-optimal solutions. This problem becomes more and more important if very fine pointing accuracy is demanded. In the alternative process proposed in this study complex parameterized FEM models are considered in the control problem from the beginning of the design. A parallel optimization (*monolithic* or *distributed*) of structures and control laws is performed. Moreover the use of the LFT framework allows the introduction of uncertainties in the model used for control synthesis such that the final controller already robustly cope with them. This methodology thus also optimizes the number of control syntheses generally done in common industrial practice, which are often based on the nominal mechanical model and some worst-cases (WC) dictated by experience. The V&V process could finally benefit of the proposed approach since powerful tool for uncertain closed-loop analysis are nowadays available. These methods, as  $\mu$ -analysis, can analytically prove the design robustness and detect very rare worst-case that could escape to Monte Carlo sample-based simulation approach.

After recalling the principles of the multi-body TITOP modeling approach in Sect. 2.1 and showing how to build the

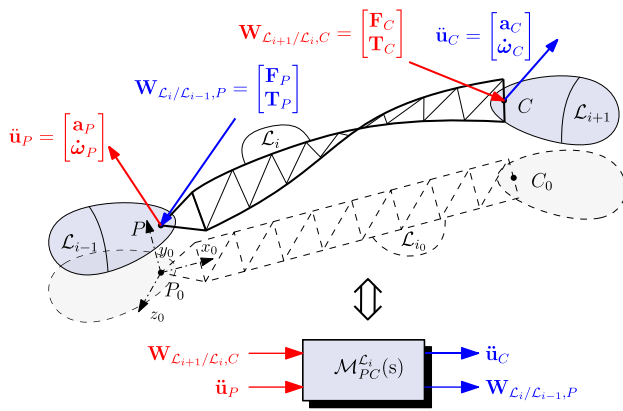


**Fig. 1**  $i$ th flexible appendage sub-structured body (top) and equivalent TITOP model (bottom)

uncertain plant of the ENVISION study case, the formulation of the robust control problem is presented in Sect. 3. Section 4 details the proposed *distributed* and *monolithic* optimization algorithms and Sect. 5 presents the achieved results by comparing the two approaches and providing formal validation of the synthesized controllers. Section 6 finally summarized all paper’s contributions.

## 2 Parametric multi-body modeling

When dealing with robust optimization of control and structural parameters of complex systems, a rigorous modeling framework able to take into account both optimization variables and system uncertainties is paramount. In the following sections the TITOP approach is presented with its direct application to the study case.

### 2.1 Two-Input Two-Output Port Theory

Let’s consider the generic flexible appendage  $\mathcal{L}_i$  in Fig. 1 linked to a parent substructure  $\mathcal{L}_{i-1}$  at point  $P$  and to a child substructure  $\mathcal{L}_{i+1}$  at point  $C$ . Moreover let us define the reference frame  $\mathcal{R}_0 = (P, x_0, y_0, z_0)$  centered in node  $P$  of  $\mathcal{L}_i$  in equilibrium condition. In the model of the appendage  $\mathcal{L}_i$ , clamped-free boundary conditions are considered: the joint at point  $P$  is rigid and statically determinate, with the parent body  $\mathcal{L}_{i-1}$  imposing a motion on  $\mathcal{L}_i$ , while point  $C$  is internal and unconstrained, and the action of  $\mathcal{L}_{i+1}$  is by means of a transmitted effort.

The TITOP model  $\mathcal{M}_{PC}^{\mathcal{L}_i}(s)$  is a linear state-space model with 12 inputs (6 for each of the two input ports):

1. The 6 components in  $\mathcal{R}_0$  of the wrench  $\mathbf{W}_{\mathcal{L}_{i+1}/\mathcal{L}_i,C}$  composed of the three-components force vector  $\mathbf{F}_C$  and the

- three-components torque vector  $\mathbf{T}_C$  applied by  $\mathcal{L}_{i+1}$  to  $\mathcal{L}_i$  at the free node  $C$ ;
2. The 6 components in  $\mathcal{R}_0$  of the acceleration vector  $\ddot{\mathbf{u}}_P$  composed of the three-components linear acceleration vector  $\mathbf{a}_P$  and the three-components angular acceleration vector  $\dot{\boldsymbol{\omega}}_P$  at the clamped node  $P$ ;

and 12 outputs (6 for each of the two output ports):

1. The 6 components in  $\mathcal{R}_0$  of the acceleration vector  $\ddot{\mathbf{u}}_C$  at the free node  $C$ ;
2. The 6 components in  $\mathcal{R}_0$  of the wrench  $\mathbf{W}_{\mathcal{L}_i/\mathcal{L}_{i-1},P}$  applied by  $\mathcal{L}_i$  to the parent structure  $\mathcal{L}_{i-1}$  at the clamped node  $P$ .

The TITOP model  $\mathcal{M}_{P,C}^{\mathcal{L}_i}(s)$  displayed in Fig. 1 (right) includes in a minimal state-space model the direct dynamic model (transfer from acceleration twist to wrench) at point  $P$  and the inverse dynamic model (transfer from wrench to acceleration twist) at point  $C$ .

This model, conceived with the clamped-free condition, is useful to study any other kind of boundary configuration as proven by Chebbi et al. (2017) thanks to the invertibility of all of its 12 input–output channels.

The TITOP model  $\mathcal{M}_{P,C}^{\mathcal{L}_i}(s)$  can be then obtained analytically for simple geometries like beams (Chebbi et al. 2017) and mechanisms (Sanfedino et al. 2022) or numerically by Finite Element Model (FEM) analysis (Sanfedino et al. 2018). In the latter case, by considering the generalized modal coordinates  $\boldsymbol{\eta}$  of the classical Craig-Bampton approach, the state-space representation of  $\mathcal{M}_{P,C}^{\mathcal{L}_i}(s)$  is given by:

$$\begin{bmatrix} \dot{\boldsymbol{\eta}} \\ \ddot{\mathbf{u}}_C \\ \mathbf{W}_{\mathcal{L}_i/\mathcal{L}_{i-1},P} \end{bmatrix} = \begin{bmatrix} \mathbf{A} & \mathbf{B} \\ \mathbf{C} & \mathbf{D} \end{bmatrix} \begin{bmatrix} \boldsymbol{\eta} \\ \dot{\boldsymbol{\eta}} \\ \mathbf{W}_{\mathcal{L}_{i+1}/\mathcal{L}_i,C} \\ \ddot{\mathbf{u}}_P \end{bmatrix}, \quad (3)$$

where

$$\begin{aligned} \mathbf{A} &= \begin{bmatrix} \mathbf{0}_{N_i \times N_i} & \mathbf{I}_{N_i} \\ -\mathbf{k} & -\mathbf{c} \end{bmatrix}, & \mathbf{B} &= \begin{bmatrix} \mathbf{0}_{N_i \times 6} & \mathbf{0}_{N_i \times 6} \\ \Phi_C^T & -\mathbf{L}_P \end{bmatrix}, \\ \mathbf{C} &= \begin{bmatrix} -\Phi_C \mathbf{k} & -\Phi_C \mathbf{c} \\ \mathbf{L}_P^T \mathbf{k} & \mathbf{L}_P^T \mathbf{c} \end{bmatrix}, \\ \mathbf{D} &= \begin{bmatrix} \Phi_C \Phi_C^T & (\boldsymbol{\tau}_{CP} - \Phi_C \mathbf{L}_P) \\ (\boldsymbol{\tau}_{CP} - \Phi_C \mathbf{L}_P)^T & \mathbf{L}_P^T \mathbf{L}_P - \mathbf{M}_{tr} \end{bmatrix}. \end{aligned}$$

- $\mathbf{k} = \text{diag}(\omega_k^2)$ : is the diagonal matrix of the square value of the retained  $N_\omega$  frequencies of the flexible modes  $\omega_k$ , with  $k \in 1 \dots N_\omega$ ;
- $\mathbf{c} = \text{diag}(2\zeta_k \omega_k)$ : damping matrix, where  $\zeta_k$  is the modal damping factor associated to mode  $\omega_k$ ;

- $\mathbf{L}_P$ : matrix of the participation factors w.r.t.  $P$ ;
- $\Phi_C$ : projections of the flexible mode shapes on  $C$ ;
- $\mathbf{M}_{rr} = \mathbf{M}_r - \mathbf{L}_P^T \mathbf{L}_P$ : residual mass, obtained from the rigid body mass matrix  $\mathbf{M}_r$ ;
- $\tau_{CP}$  describes the rigid kinematic model between the DOFs of the generic internal node  $C$  and the junction DOFs of the node  $P$ . For a clamped (in  $P$ ) - free (in  $C$ ) flexible structure:

$$\tau_{CP} = \begin{bmatrix} \mathbf{I}_3 & * \overrightarrow{\mathbf{CP}} \\ \mathbf{0}_3 & \mathbf{I}_3 \end{bmatrix}, \tag{4}$$

where  $* \overrightarrow{\mathbf{CP}}$  is the skew-symmetric matrix associated with the vector from  $C$  to  $P$  of the flexible appendage in the undeformed configuration.

All the parameters needed to build the model (3) can be recovered by running a modal analysis with a commercial software like MSC NASTRAN. A particularity of TITOP models is to have access to each structural parameter in an analytical way and have the possibility to easily assign it an uncertainty. In this way the model can be straightforward put in a generalized LFT form, directly exploitable for modern robust control synthesis/analysis techniques. If in fact we consider for instance that now in model (3) at each modal frequency  $\omega_k$  is associated a parametric uncertainty  $\delta\omega_k \in [-1, 1]$  such that the uncertain frequency is now expressed as  $\tilde{\omega}_k = \omega_k (1 + \delta\omega_k)$ , the corresponding TITOP model  $\mathcal{M}_{P,C}^{L_i}(s, \mathbf{\Delta})$  (with  $\mathbf{\Delta} = \text{diag}(\delta\omega_k)$ ) can be represented by the block diagram as in Fig. 2 (left side) with a minimal number of repetitions of the uncertainties. Note that parameters to be optimized can be isolated in the same way.

In the same figure the equivalent LFT model is shown on the right side, where the uncertain blocks can be isolated with respect to the nominal plants thanks to the exogenous inputs  $\mathbf{w}$  and outputs  $\mathbf{z}$ , obtained by opening  $\mathcal{M}_{P,C}^{L_i}(s, \mathbf{\Delta})$  respectively in the points marked in red and blue in Fig. 2 (left).

The TITOP approach was finally extended to multiple ports in case several child structures are connected to the  $i$ th flexible sub-structure (Sanfedino et al. 2018).

### 2.2 Spacecraft assembly

Once a TITOP model is obtained for each sub-structure of a multi-body system, the assembly is easily done by connecting the ports corresponding to the connection points among the sub-elements. Let's consider the ENVISION spacecraft depicted in Fig. 3. It is constituted by a rigid central body  $\mathcal{B}$ , two solar arrays  $\mathcal{S}_1$  and  $\mathcal{S}_2$ , a Subsurface Radar System (SRS) composed of two flexible beams  $\mathcal{Q}_1$  and  $\mathcal{Q}_2$ , and a Synthetic

Aperture Radar (SAR)  $\mathcal{V}$ . In Fig. 3 it can be noticed that the central body reference frame is centered in its center of mass (CoM)  $B$ , while all appendages have their body frame defined in correspondence of their attachment nodes.

The assembled model of the whole spacecraft in TITOP framework is shown in Fig. 4. Note that each sub-components has its corresponding LFT block connected to the other block throw wrench of forces/torques and linear/angular accelerations. In particular:

- the central body  $\mathcal{B}$  is modeled as a Multi-Port Rigid Body in which all inputs are the wrenches applied to all connection points by the appendages and the resultant wrench of the external perturbation forces/torques  $[\mathbf{W}_{\text{ext},\mathcal{B},B}]_{\mathcal{R}_B}$  applied to its CoM  $B$ . See Sanfedino (2019) for more details on this model;
- the two solar panels, the two beams constituting the SRS antenna and the SAR antenna are modeled as generic flexible structures built from NASTRAN FEM analysis as discussed in Sect. 2.1.

Note that in Fig. 4 the dynamical models of the appendages are connected to the main body structure through the rotation matrices  $\mathbf{P}_{a(0)/b}^{\times 2}$  that express the wrench vectors expressed in the body frame of appendage  $\mathcal{A}$  into the body frame of the main body  $\mathcal{B}$ . The transpose of these matrices allows projecting the acceleration vectors instead. Since the solar arrays are not fixed on the ENVISION platform, the rotation matrices  $\mathbf{R}^{\times 2}(\theta_{SA}, \mathbf{y}_{s,*})$ , dependent on the solar array configuration angle  $\theta_{SA}$  around the rotation axis  $\mathbf{y}_{s,*}$ , take into account the presence of a Solar Array Drive Mechanism (SADM) and can be easily expressed in a LFT way as shown in Dubanchet (2016), where the considered uncertain parameter is  $\sigma_4 = \tan(\theta_{SA}/4)$ , such that  $\mathbf{\Delta}_{\sigma_4} = \sigma_4 \mathbf{I}_8$ . Finally all other uncertain blocks  $\mathbf{\Delta}_*$  take into account all possible uncertainties and optimization parameters associated to each substructure.

The main advantages of having the system expressed in TITOP framework are listed below:

- physical understanding is conserved at sub-component level;
- parametric uncertainty can be considered at sub-component level;
- redesign of sub-component in preliminary design phase is easy;
- adaptability to a user-friendly Matlab/Simulink toolbox. The Satellite Dynamics Toolbox library (SDTlib) allows to easily model dynamical space systems in TITOP approach (Alazard and Sanfedino 2020).

The assembled TITOP model is validated with an equivalent model built in Simscape, where Reduced Order Flexible

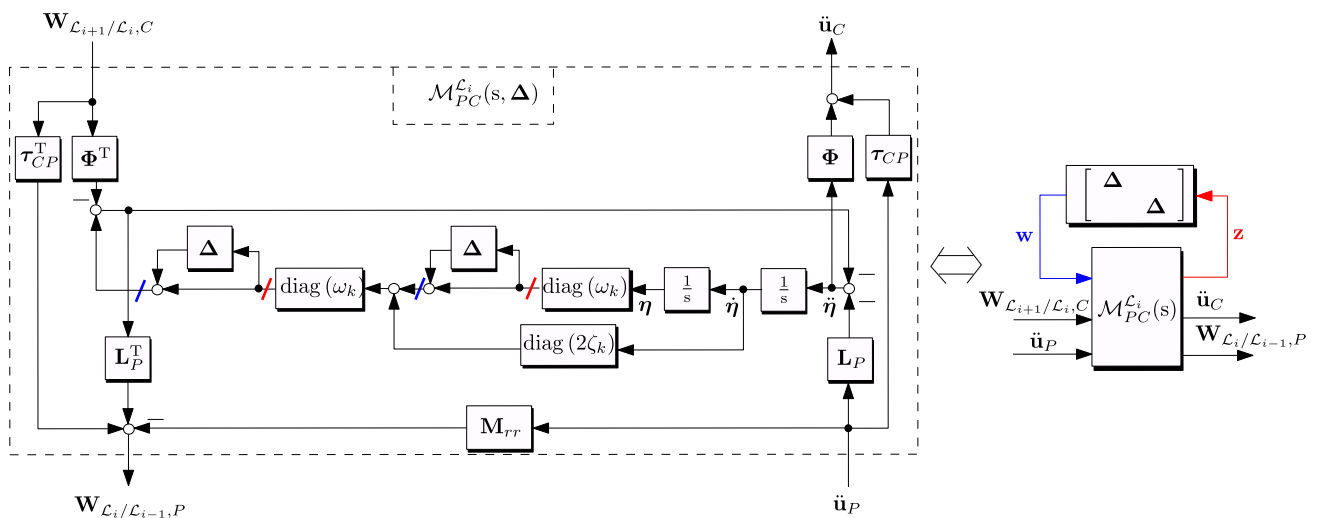


**Fig. 2** Uncertain TITOP model of a generic flexible structure based on FEM modal analysis (left) and its equivalent LFT form (right). (Color figure online)

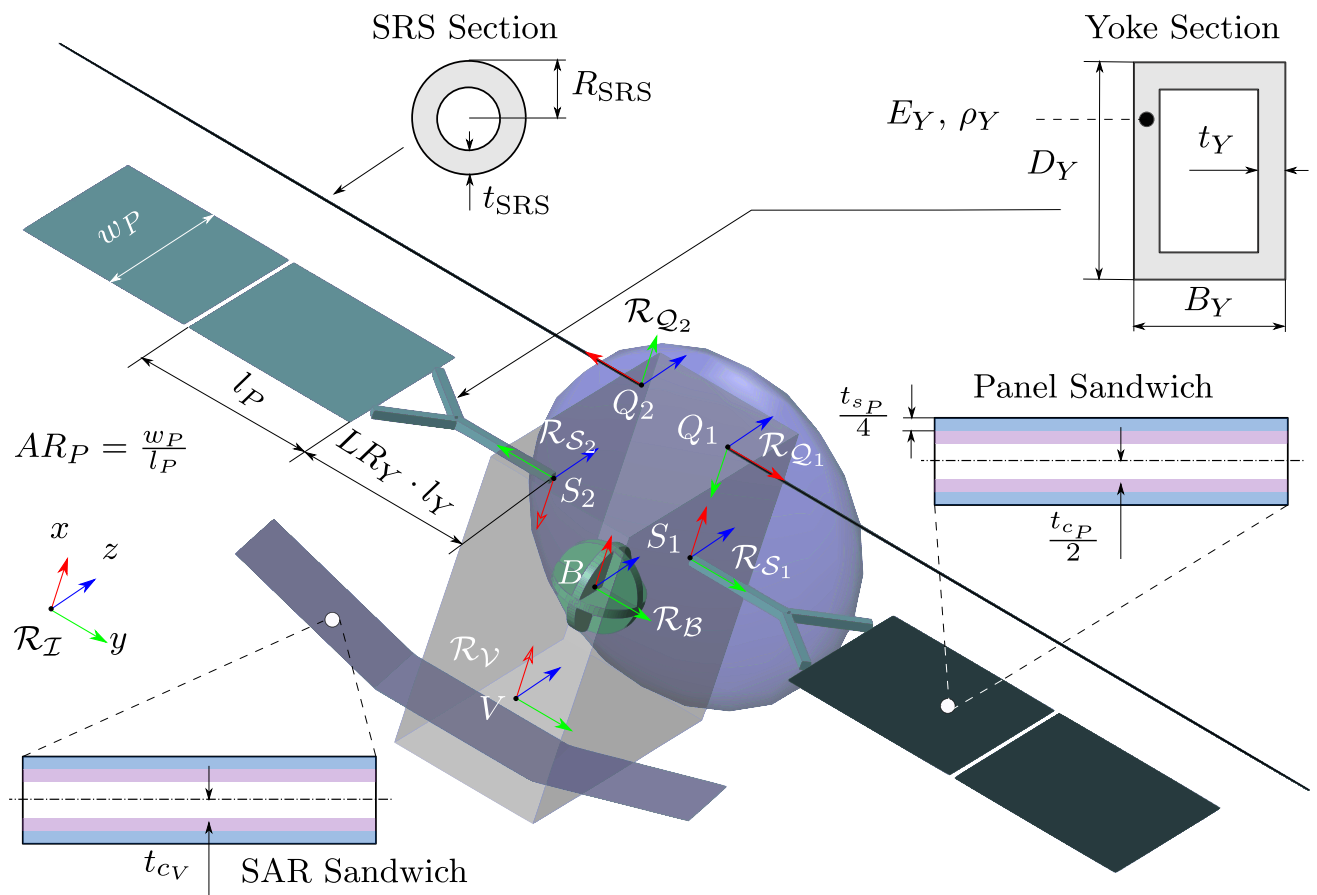


**Fig. 3** ENVISION spacecraft: definition of geometry and reference frames

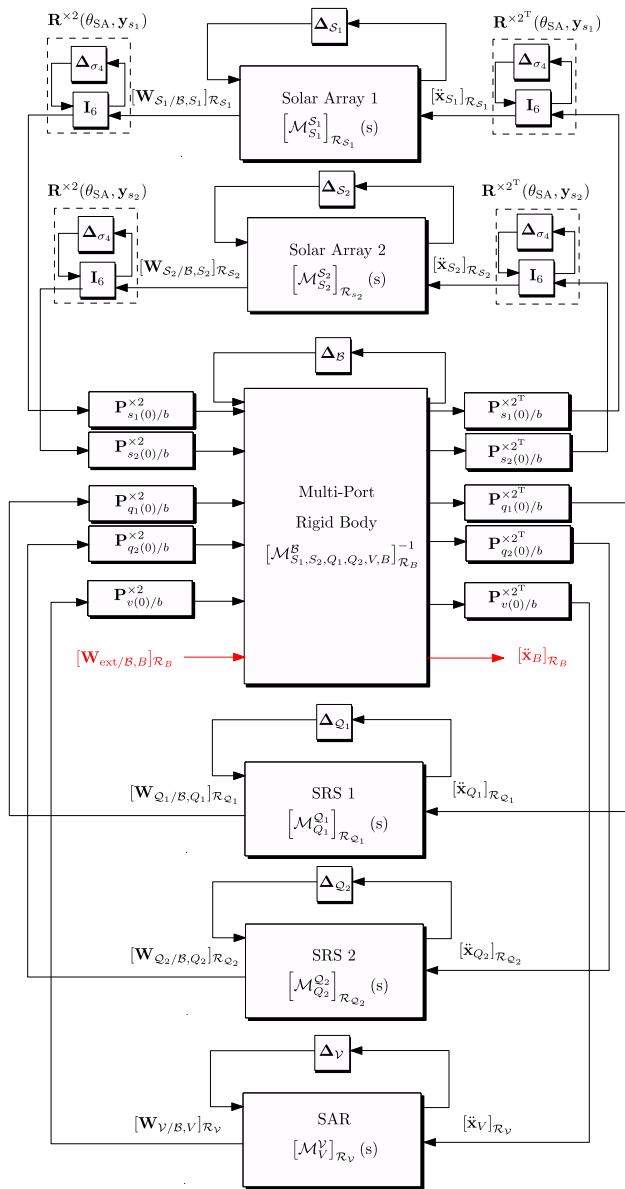


**Fig. 4** Assembled dynamics of the ENVISION spacecraft in TITOP framework

Solid (ROFS) blocks are used for all flexible appendages. In order to correctly parameterize the constitutive mass, stiffness and damping matrices directly for a NASTRAN FEM analysis, the approach presented in Alazard et al. (2023) is used. Note that the number of flexible modes considered for each flexible appendage is 10 in order to have a satisfactory modal effective mass fraction and not an excessive number of states at the same time. A comparison of the  $3 \times 3$  transfer functions  $[W_{ext/B,B}]_{R_B} (4 : 6) \rightarrow [x_B]_{R_B} (4 : 6)$  from the three external torques applied at point  $B$  to the three angular accelerations experienced by point  $B$ , is shown in Fig. 5. Notice as SDTlib and Simscape models are close and their difference is several orders of magnitude smaller than

their absolute values. This comparison is based on the same nominal configuration of the ENVISION plant, where all parametric variation are fixed to a particular value.

The introduction of uncertainties in TITOP formalism then makes SDTlib model directly exploitable for robust control synthesis/analysis and *monolithic* optimization.

### 2.2.1 Open-loop parametric analysis

An advantage of having an LFT model is that a large family of possible plants is available in a continuous way in a unique representation. In this way, it is possible to see, for instance, which parameters will impact the mass the most. By considering the ranges of the optimization parameters in Table 2 for the ENVISION benchmark, the potential gain in spacecraft overall mass after optimization is shown in Fig. 6. We notice, in particular, as the thickness of the composite sandwiches constituting the solar panels ( $t_{cp}$  and  $t_{sp}$ ) and the SAR antenna ( $t_{cv}$ ) are the most sizing. In the context of co-design of structure and control architecture it is also important to see the impact of the design parameters on the system flexibility. Some natural modes can in fact interact with the control bandwidth by causing a significant degradation of the control stability/performance. Figure 7 shows the singular values of the transfer function  $[W_{ext/B,B}]_{R_B} \rightarrow [x_B]_{R_B}$  when one optimization parameter varies in its admissible range and all other optimization parameters impacting the mass are fixed to their maximum value. When not varying, the panel aspect ratio and the yoke length ratio are equal to unity and the Yoke Young Modulus takes its minimum value. Note that the situation in which all parameters are fixed is marked in magenta and no uncertainty is considered in this analysis. Only the most impacting parameters provoking a shift of normal modes is depicted in Fig. 7: i.e. a reduction of the SRS outer radius  $R_{SRS}$  or the side lengths ( $B_Y$  and  $D_Y$ ) of the Yoke section make the first modes shift to lower frequencies.

Another phenomenon captured by the TITOP modeling is the shift of natural modes caused by the rotation of the two solar arrays. Figure 8 shows for instance the evolution of the frequency of the 6th and 8th mode when both  $B_Y$  and  $\theta_{SA}$  vary.

### 2.2.2 Modeling uncertainty for distributed and monolithic optimization

When dealing with *distributed* optimization, the decoupling between the global structural problem from the nested control optimization, shown in Eq. (2), requires that the optimization structural variables  $y_s$  are fixed during control synthesis. For this reason, in the *distributed* optimization the overall uncertain block  $\Delta^{SC}$ , obtained by putting the model depicted in Fig. 4 in the generalized LFT form, contains only the set of real uncertainties listed in Table 1. When a *monolithic* opti-

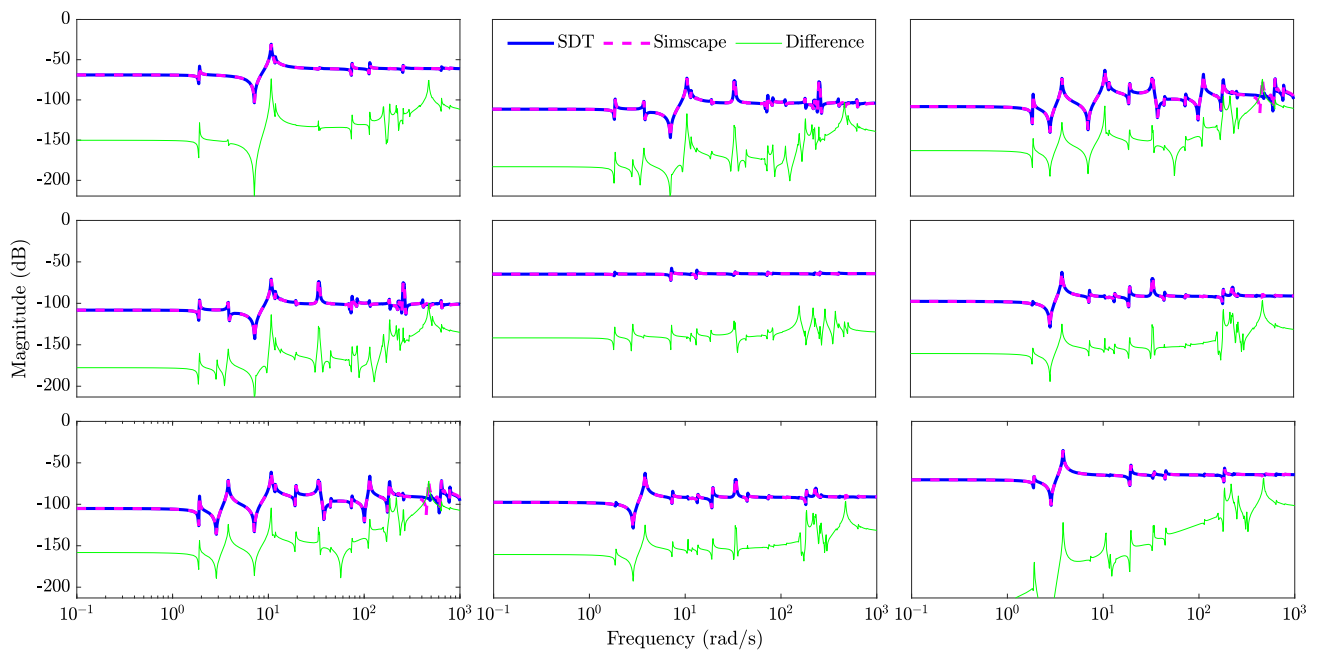


**Fig. 5** Comparison of SDT and Simscape models of the transfer function  $[\mathbf{W}_{\text{ext}/B,B}]_{\mathcal{R}_B} (4 : 6) \rightarrow [\mathbf{\ddot{x}}_B]_{\mathcal{R}_B} (4 : 6)$

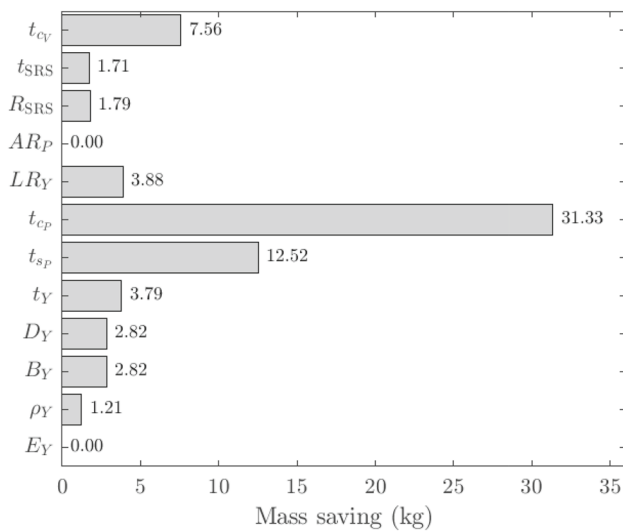


**Fig. 6** Potential mass saving (in kg) obtained by optimization of the ENVISION design parameters

mization routine is chosen instead, an uncertain block  $\Pi^{SC}$  containing the optimization variable is considered as well. In the *monolithic* approach in fact, as shown in Sect. 3, the non-smooth optimization routine used for robust control synthesis (Apkarian et al. 2007) is able to provide the optimized control and structural parameters at the same time by coping with all considered system uncertainties. The two different LFT models are shown in Fig. 9.

An important task to be accomplished before running a *monolithic* optimization is to correctly model the uncertain

block  $\Pi^{SC}$ . The major difficulty in this task is to keep the number of uncertainty repetitions as small as possible in order to not run into numerical problem when the robust control synthesis is tackled. When using a complex FEM model, this number can grow very fast with the number of the nodes in the mesh. For this reason, only four optimization parameters are selected in the list in Table 2, mostly impacting the overall mass and the shift of the first modes to lower frequencies: panel skin  $t_{sp}$  and core thickness  $t_{cp}$ , SRS section outer radius  $R_{SRS}$  and the SAR core thickness  $t_{cv}$ . The way adopted in this work to face this problem is to get a multivariate polynomial approximation  $\Pi^{SC}$  by using a set of samples and solving a classical Linear Least-Squares problem as proposed by Poussot-Vassal and Roos (2012). The algorithm available in the *lsapprox* routine of the APRICOT library Roos et al. (2014) is used to get an approximation of the delta-blocks for the matrices  $\mathbf{M}_{rr}$ ,  $\mathbf{L}_p$  and  $\text{diag}(\omega_k)$  in Fig. 2. A limited number of models is needed to generate a very precise approximation (order of magnitude of maximum relative error equal to  $10^{-2}$ ): 100 different NASTRAN models are generated with random values of  $t_{sp}$  and  $t_{cp}$  in their ranges and by including the four corner scenarios, 10 NASTRAN models are obtained for the SRS beam antennas by linearly spanning  $R_{SRS}$  and 10 different NASTRAN models of the SAR antenna are finally generated by linearly spanning  $t_{cv}$ . Once assembled, the  $\Pi^{SC}$  block contains the following number of occurrences: 220 for  $t_{sp}$ , 248 for  $t_{cp}$ , 64 for  $R_{SRS}$  and 116 for  $t_{cv}$ . Figure 10 shows the singular values of the final LFT model of the ENVISION spacecraft



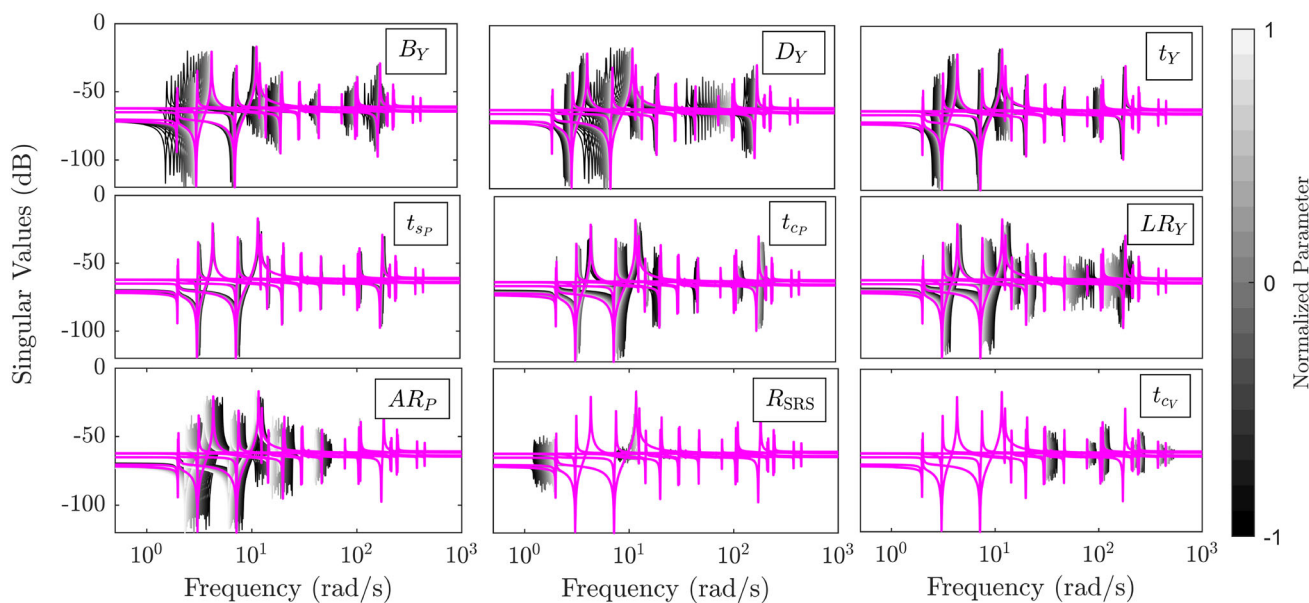


Fig. 7 Evolution of the singular values of the transfer function  $[W_{ext/B,B}]_{\mathcal{R}_B} \rightarrow [\ddot{x}_B]_{\mathcal{R}_B}$  with variation of the optimization parameters

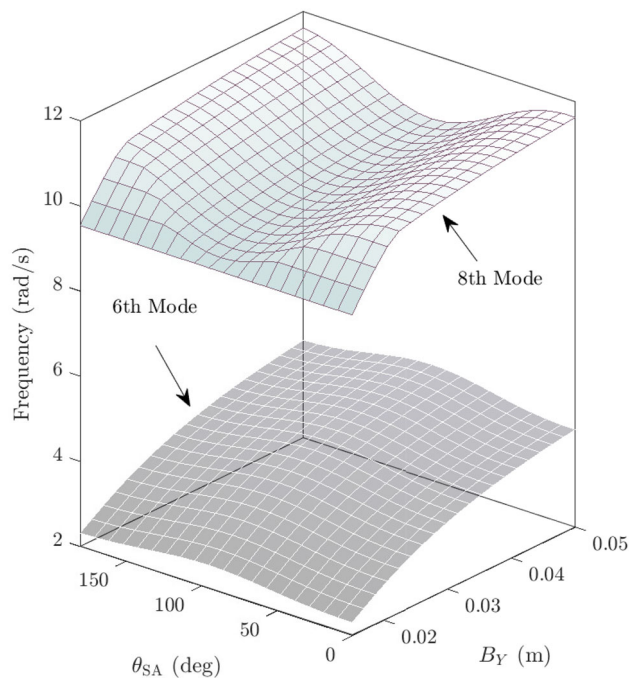


Fig. 8 Evolution of 6th and 8th mode frequencies with variation of  $B_Y$  and  $\theta_{SA}$

used for *monolithic* optimization by taking into account all uncertainties and optimization parameters.

### 3 Robust attitude control

The objective of this section is to present the general control architecture of the ENVISION Attitude Control System

Table 1 Parametric uncertainties of the ENVISION spacecraft

Parameter	Description	Occurrence	Uncertainty
$m^{\mathcal{B}}$	Mass $\mathcal{B}$	3	$\pm 15\%$
$I_{xx}^{\mathcal{B}}$	Inertia x-axis $\mathcal{B}$	1	$\pm 15\%$
$I_{yy}^{\mathcal{B}}$	Inertia y-axis $\mathcal{B}$	1	$\pm 15\%$
$I_{zz}^{\mathcal{B}}$	Inertia z-axis $\mathcal{B}$	1	$\pm 15\%$
$\omega_1^{\mathcal{S}_\bullet}$	1st mode $\mathcal{S}_\bullet$	4	$\pm 25\%$
$\omega_2^{\mathcal{S}_\bullet}$	2nd mode $\mathcal{S}_\bullet$	4	$\pm 25\%$
$\omega_1^{\mathcal{V}}$	1st mode $\mathcal{V}$	2	$\pm 25\%$
$\omega_2^{\mathcal{V}}$	2nd mode $\mathcal{V}$	2	$\pm 25\%$
$\sigma_4$	Configuration $\mathcal{S}_\bullet$	32	$[-1 \ 1]$

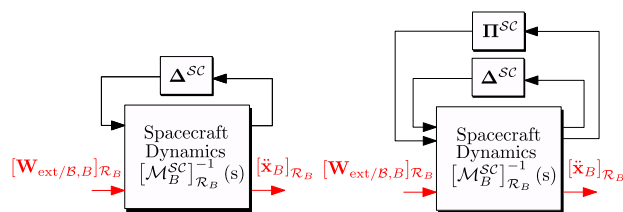


Fig. 9 LFT model of the ENVISION spacecraft used for *distributed* (left) and *monolithic* (right) optimization

(ACS). The requirements considered for this design take into account the needed resolution for the multispectral imaging cameras, the authority of the reaction wheel system and the expected multi-input multi-output (MIMO) stability margins.

We consider the robust design of a 3-axis structured MIMO attitude control law to meet:

**Table 2** Optimization structural parameters

Parameter	Symbol	Unit	Min value	Max value	Distributed opt	Monolithic opt
Yoke Young modulus	$E_Y$	Pa	$1.1 \times 10^{11}$	$1.23 \times 10^{11}$	$1.121 \times 10^{11}$	$(1.165 \times 10^{11})$
Yoke density	$\rho_Y$	kg/m <sup>3</sup>	$2.18 \times 10^3$	$4.5 \times 10^3$	$4.186 \times 10^3$	$(3.340 \times 10^3)$
Yoke section length	$B_Y$	m	$1.5 \times 10^{-2}$	$5 \times 10^{-2}$	$1.544 \times 10^{-2}$	$(3.25 \times 10^{-2})$
Yoke section height	$D_Y$	m	$1.5 \times 10^{-2}$	$5 \times 10^{-2}$	$1.502 \times 10^{-2}$	$(3.25 \times 10^{-2})$
Yoke section thickness	$t_Y$	m	$1 \times 10^{-3}$	$2 \times 10^{-3}$	$1.017 \times 10^{-3}$	$(1.5 \times 10^{-3})$
Panel skin thickness	$t_{sp}$	m	$2 \times 10^{-4}$	$4 \times 10^{-4}$	$2.042 \times 10^{-4}$	$2 \times 10^{-4}$
Panel core thickness	$t_{cp}$	m	$1 \times 10^{-2}$	$3.5 \times 10^{-2}$	$1.322 \times 10^{-2}$	$1 \times 10^{-2}$
Yoke length ratio	$LR_Y$	—	0.42	1	1	(0.71)
Panel aspect ratio	$AR_P$	—	3/4	4/3	1.237	(25/24)
SRS section outer radius	$R_{SRS}$	m	$1.25 \times 10^{-2}$	$2 \times 10^{-2}$	$1.25 \times 10^{-2}$	$1.25 \times 10^{-2}$
SRS section thickness	$t_{SRS}$	m	$3.8 \times 10^{-4}$	$6 \times 10^{-4}$	$4.959 \times 10^{-4}$	$(4.9 \times 10^{-4})$
SAR core thickness	$t_{cv}$	m	$5 \times 10^{-4}$	$1.5 \times 10^{-3}$	$5.178 \times 10^{-4}$	$1.5 \times 10^{-3}$

For the *monolithic* optimization the values in brackets correspond to the set of fixed parameters

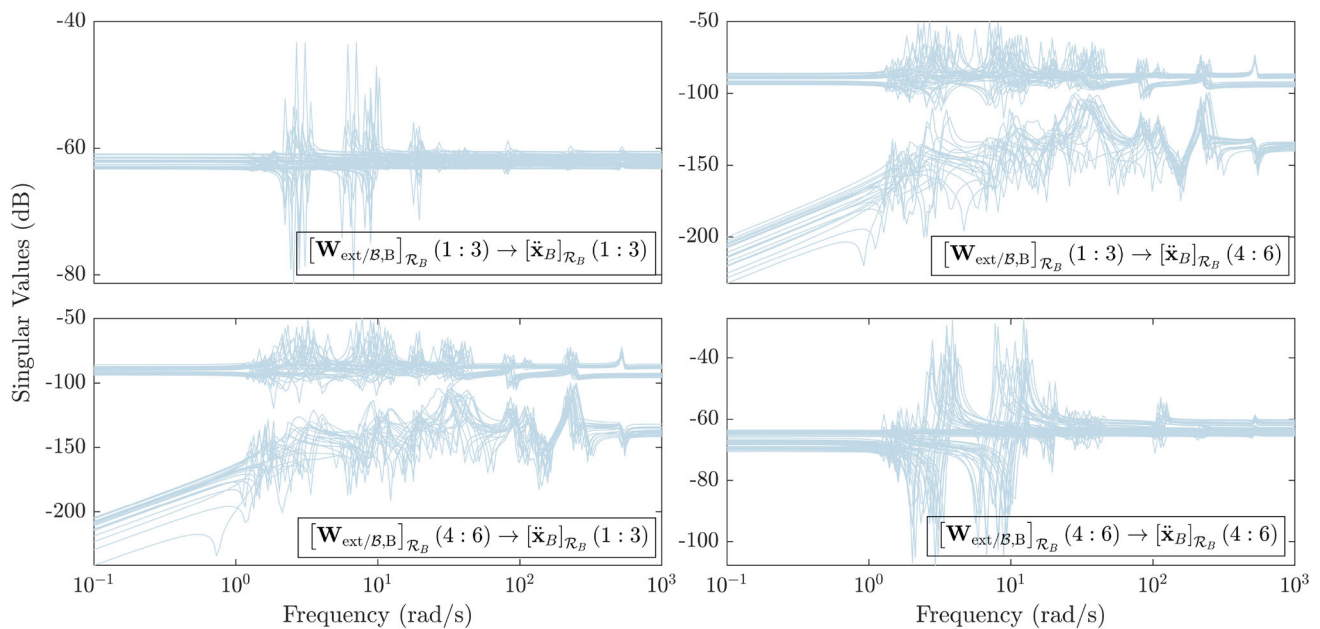


**Fig. 10** LFT model of the ENVISION plant by considering all uncertainties and optimization parameters for *monolithic* optimization

- **(Req1)** the absolute pointing requirement, defined by the  $3 \times 1$  vector of Absolute Performance Error ( $\mathbf{APE} = [0.08 \ 0.2 \ 0.08]^T \times 10^{-3}$  rad), in spite of low frequency orbital disturbances dominated by the gravity gradient torque (characterized by the  $3 \times 1$  upper bound on the magnitude  $\mathbf{T}_{ext} = [1.9 \ 1.9 \ 1.9]^T \times 10^{-3}$  Nm),
- **(Req2)** the relative pointing requirement, defined by the  $3 \times 1$  vector of Relative Performance Error ( $\mathbf{RPE} = [0.5 \ 0.5 \ 0.5]^T \times 10^{-3}$  rad) to be kept for a time window  $\Delta t_{RPE} = 15$  s,
- **(Req3)** the maximum command requirement, defined by the  $3 \times 1$  vector of maximum control torque ( $\bar{\mathbf{u}} = [0.215 \ 0.215 \ 0.215]^T$  Nm),

- **(Req4)** stability margins characterized by an upper bound  $\gamma$  on the  $\mathcal{H}_\infty$ -norm of the input sensitivity function,

while minimizing the variance of the APE and RPE in response to the star sensor and gyro noises characterized by their Power Spectral Density (PSD), respectively  $\mathbf{PSD}^{SST} = (3.5 \times 10^{-5})^2 \mathbf{I}_3 \text{ rad}^2 \text{ s}$  and  $\mathbf{PSD}^{GYRO} = (1.4 \times 10^{-6})^2 \mathbf{I}_3 \text{ rad}^2/\text{s}$  (assumed to be equal for the 3 components).

The value  $\gamma = 1.5$  ensures on each of the 3 axes:

- a disk margin  $> 1/\gamma = 0.667$ ,
- a gain margin  $> \frac{\gamma}{\gamma-1} = 3$  (9.542 dB),

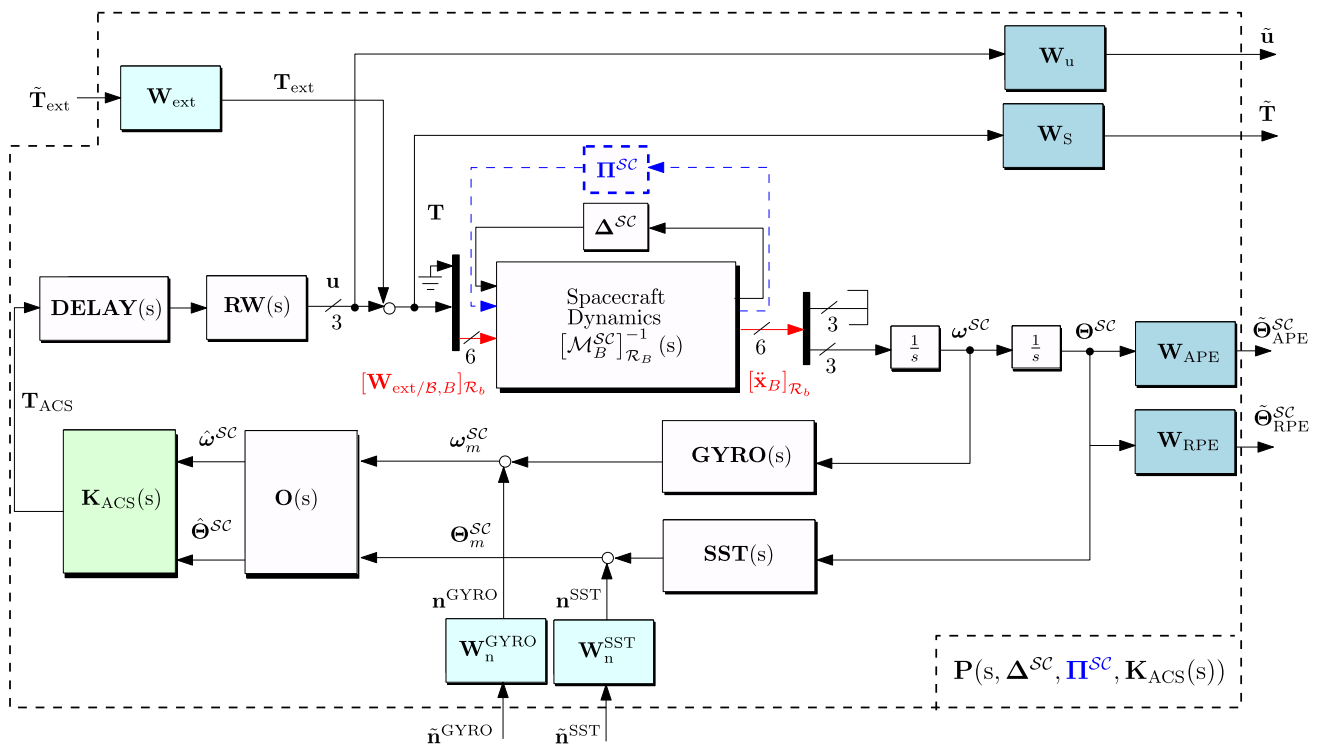


Fig. 11 Attitude control system architecture

- a phase margin  $> 2 \arcsin \frac{1}{2\gamma} = 38.9^\circ$ .

The requirements **Req1**, **Req2** and **Req3** must be met for any values of the uncertain mechanical parameters regrouped in the block  $\Delta^{SC}$ .

By referring to Fig. 11, the models of the avionics components are:

- A reaction wheel system modeled as a second order dynamics with cut-off natural frequency of  $100\pi$  rad/s and damping factor 0.7:

$$\mathbf{RW}(s) = \frac{(100\pi)^2}{s^2 + 140\pi s + (100\pi)^2} \mathbf{I}_3 \quad (5)$$

- A gyro sensor modeled as a first-order dynamics with cut-off frequency  $200\pi$  rad/s:

$$\mathbf{GYRO}(s) = \frac{200\pi}{s + 200\pi} \mathbf{I}_3 \quad (6)$$

- A star sensor modeled as a first-order dynamics with cut-off frequency  $16\pi$  rad/s:

$$\mathbf{SST}(s) = \frac{16\pi}{s + 16\pi} \mathbf{I}_3 \quad (7)$$

- A loop delay modeled as a 2nd order Pade approximation with time delay  $T_d = 0.0625$  s:

$$\mathbf{DELAY}(s) = \frac{T_d^2 s^2 - 6T_d s + 12}{T_d^2 s^2 + 6T_d s + 12} \mathbf{I}_3 \quad (8)$$

A gyro-stellar observer  $\mathbf{O}(s)$  is used to filter the gyro and the star sensor measurements. Its state-space realization is given by:

$$\begin{cases} \dot{\mathbf{x}}_O = \begin{bmatrix} -0.1131 & -1 \\ 0.003948 & 0 \end{bmatrix} \mathbf{x}_O + \begin{bmatrix} 0.1131 & 1 \\ -0.00394 & 0 \end{bmatrix} \begin{bmatrix} \omega_m^{SC} \\ \Theta_m^{SC} \end{bmatrix} \\ \begin{bmatrix} \hat{\omega}^{SC} \\ \hat{\Theta}^{SC} \end{bmatrix} = \begin{bmatrix} 1 & 0 \\ -0.1131 & -1 \end{bmatrix} \mathbf{x}_O + \begin{bmatrix} 0 & 0 \\ 0.1131 & 1 \end{bmatrix} \begin{bmatrix} \omega_m^{SC} \\ \Theta_m^{SC} \end{bmatrix} \end{cases} \quad (9)$$

with  $\mathbf{x}_O$  the observer state vector.

The closed-loop generalized plant  $\mathbf{P}(s, \Delta^{SC}, \Pi^{SC}, \mathbf{K}_{ACS}(s))$  used for the robust control synthesis is shown in Fig. 11. Note that for *distributed* optimization the block  $\Pi^{SC}$  has not to be taken into account.

The following weighting filters are used to normalize the inputs and outputs:  $\mathbf{W}_{ext} = \mathbf{T}_{ext}$ ,  $\mathbf{W}_n^{SST} = \sqrt{\mathbf{PSD}^{SST}}$ ,  $\mathbf{W}_n^{GYRO} = \sqrt{\mathbf{PSD}^{GYRO}}$ ,  $\mathbf{W}_{APE} = (\text{diag}(\mathbf{APE}))^{-1}$ ,  $\mathbf{W}_{RPE} = (\text{diag}(\mathbf{RPE}))^{-1} \frac{\Delta_{RPE}(\Delta_{RPE} + \sqrt{12})}{\Delta_{RPE}^2 s^2 + 6\Delta_{RPE} s + 12}$  and  $\mathbf{W}_S = \frac{1}{\gamma} \mathbf{I}_3$ .

Finally the block  $\mathbf{K}_{ACS}(s)$  represents the structured  $3 \times 6$  attitude controller to be synthesized. The chosen structure

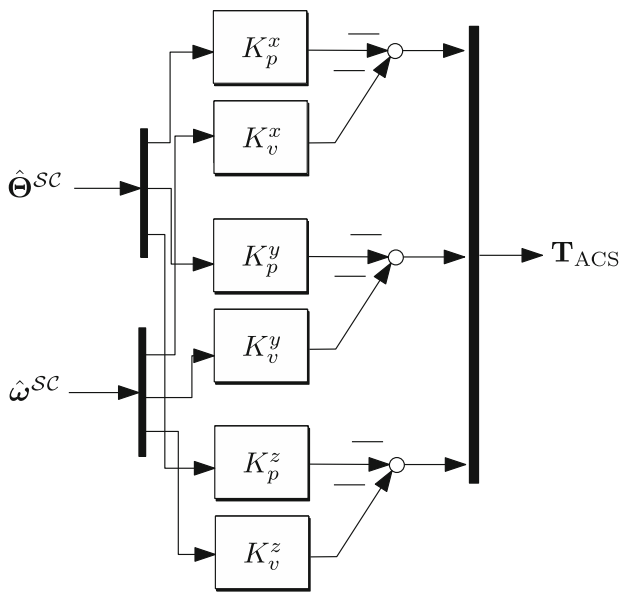


Fig. 12 Structured controller  $\mathbf{K}_{ACS}(s)$

is shown in Fig. 12. It is a decentralized proportional-derivative controller (the gains  $K_p^i$  and  $K_v^i$ ,  $i = x, y, z$ )

The set of the 6 controller tunable parameters ( $K_p^i$ ,  $w^i$  and  $K_v^i$ ,  $i = x, y, z$ ) are roughly initialized assuming a rigid 3-axis decoupled spacecraft and in order to:

- reject a constant orbital disturbance  $\mathbf{T}_{ext}$  with a steady state pointing error  $\Theta^{SC}$  lower than the  $APE(i)$  requirement on each axis  $i = x, y, z$ ,
- tune the 2nd order closed-loop dynamics of each axis with a damping ratio  $\xi = 0.7$  and a given frequency bandwidth  $\omega^i$  ( $\omega^i = 0.06$  rad/s,  $i = x, y, z$ ).

Indeed, under these assumptions, the open-loop model between the control torque and the pointing error is equal to  $\frac{1}{\mathbf{J}_B^{SC} s^2}$ , where the nominal  $3 \times 3$  inertia  $\mathbf{J}_B^{SC}$  on the whole spacecraft at point  $B$  can be computed from the DC gain of the nominal model  $[\mathcal{M}_B^{SC}]_{\mathcal{R}_B}^{-1}(s)$ :

$$\mathbf{J}_B^{SC} = \left[ [\mathcal{M}_B^{SC}]_{\mathcal{R}_B}^{-1}(0) \right]^{-1} \quad (4 : 6; 4 : 6) \quad (10)$$

Then the tuning:

$$\begin{aligned} K_p^i &= \mathbf{J}_B^{SC}(i, i) \omega_i^r{}^2 \\ K_v^i &= 2 \xi \mathbf{J}_B^{SC}(i, i) \omega_i^r \end{aligned} \quad (11)$$

with  $\omega_i^r$  required bandwidth on  $i$ th axis ( $i = 1, 2, 3$ ), ensures the needed closed-loop dynamics and a disturbance rejection

function expressed as:

$$\frac{\Theta^{SC}(i)}{\mathbf{T}_{ext}(i)}(s) = \frac{1}{\mathbf{J}_B^{SC}(i, i)} \frac{1}{s^2 + 2 \xi \omega_i^r s + \omega_i^r{}^2} \quad (12)$$

Thus the required bandwidth  $\omega_i^r$  to meet the absolute pointing error requirement in steady state ( $\Theta^{SC}(i) \leq APE(i)$ ) is:

$$\omega_i^r \geq \sqrt{\frac{\mathbf{T}_{ext}(i)}{\mathbf{J}_B^{SC}(i, i) APE(i)}} \quad (13)$$

This initial tuning, based on simplified assumptions is useful to initialize the non-convex optimization control problem. A robust controller is in fact synthesized thanks to the `systeme` routine available in MATLAB, based on the non-convex optimization algorithm proposed by Apkarian et al. (2015).

For the control synthesis two cases have to be distinguished according to the type of optimization architecture.

### 3.1 Distributed optimization

In the case of *distributed* optimization all structural optimization parameters are fixed for each control synthesis. In that case the nested mixed  $\mathcal{H}_2/\mathcal{H}_\infty$  control optimization problem is directly formulated from the objective (Eq. (14)) and the constraints (Eq. (15)) defined in Sect. 3. The objective is in fact to minimize the  $\mathcal{H}_2$ -norm (or the variance) of the transfer from all measurements noises to the pointing requirements for the worst-case uncertainty configuration by coping with a set of hard constraints, expressed in terms of  $\mathcal{H}_\infty$ -norm.

### 3.2 Monolithic optimization

In the case a *monolithic* optimization architecture is chosen, the non-convex control synthesis algorithm can handle both control and structure optimization at the same time. In this case the hard constraints (17) are exactly the same as in the *distributed* optimization. However the multi-objectives problem shown in Eq. (16) (where  $\bar{\sigma}(\bullet)$  represents the upper bound singular value) has to be solved instead.

Note that the second objective (where the notation of the projections in body frame has been omitted for better clarity), translates the minimization of the overall spacecraft nominal mass. The transfer function  $\left[ [\mathcal{M}_B^{SC}]_{\mathbf{w}_{ext/B,B}(1) \rightarrow \ddot{\mathbf{x}}_B(1)}^{-1}(\omega, \mathbf{\Delta}^{SC}, \mathbf{\Pi}^{SC}) \right]^{-1}$  for  $\omega \in [0, 0.0001]$  represents in fact the DC gain (or the low frequency response) of the inverted transfer from the force to acceleration along the  $x$ -axis, that is the nominal mass of the overall spacecraft.

**(I) Nested Control Optimization for *distributed* Optimization Architecture:**

$$J_{c1} = \min_{\mathbf{K}_{ACS}} \max_{\Delta^{SC}} \left\| \mathbf{P} \begin{bmatrix} \tilde{\mathbf{n}}^{GYRO} \\ \tilde{\mathbf{n}}^{SST} \end{bmatrix} \rightarrow \begin{bmatrix} \tilde{\Theta}_{APE}^{SC} \\ \tilde{\Theta}_{RPE}^{SC} \end{bmatrix} (s, \Delta^{SC}, \mathbf{K}_{ACS}) \right\|_2 \leq 1 \tag{14}$$

such that:

$$\begin{aligned} J_{c2} &= \max_{\Delta^{SC}} \left\| \mathbf{P}_{\tilde{\mathbf{T}}_{ext} \rightarrow \tilde{\Theta}_{APE}^{SC}} (s, \Delta^{SC}, \mathbf{K}_{ACS}) \right\|_{\infty} \leq 1 \quad \text{(Req1)} \\ J_{c3} &= \max_{\Delta^{SC}} \left\| \mathbf{P}_{\tilde{\mathbf{T}}_{ext} \rightarrow \tilde{\Theta}_{RPE}^{SC}} (s, \Delta^{SC}, \mathbf{K}_{ACS}) \right\|_{\infty} \leq 1 \quad \text{(Req2)} \\ J_{c4} &= \max_{\Delta^{SC}} \left\| \mathbf{P}_{\tilde{\mathbf{T}}_{ext} \rightarrow \tilde{\mathbf{u}}} (s, \Delta^{SC}, \mathbf{K}_{ACS}) \right\|_{\infty} \leq 1 \quad \text{(Req3)} \\ J_{c5} &= \max_{\Delta^{SC}} \left\| \mathbf{P}_{\tilde{\mathbf{T}}_{ext} \rightarrow \tilde{\mathbf{T}}} (s, \Delta^{SC}, \mathbf{K}_{ACS}) \right\|_{\infty} \leq 1 \quad \text{(Req4)} \end{aligned} \tag{15}$$

**(II) Control/Structure Co-Optimization for *monolithic* Optimization Architecture:**

$$\left\{ \begin{aligned} &\min_{\mathbf{K}_{ACS}, \Pi^{SC}} \max_{\Delta^{SC}} \left\| \mathbf{P} \begin{bmatrix} \tilde{\mathbf{n}}^{GYRO} \\ \tilde{\mathbf{n}}^{SST} \end{bmatrix} \rightarrow \begin{bmatrix} \tilde{\Theta}_{APE}^{SC} \\ \tilde{\Theta}_{RPE}^{SC} \end{bmatrix} (s, \Delta^{SC}, \Pi^{SC}, \mathbf{K}_{ACS}) \right\|_2 \leq 1 \\ &\min_{\mathbf{K}_{ACS}, \Pi^{SC}} \max_{\Delta^{SC}} \bar{\sigma} \left( \left[ [\mathcal{M}_B^{SC}]_{W_{ext}/B, B(1) \rightarrow \ddot{x}_B(1)}^{-1} (j\omega, \Delta^{SC}, \Pi^{SC}) \right]^{-1} \right), \quad \forall \omega \in [0, 0.0001] \end{aligned} \right. \tag{16}$$

such that:

$$\begin{aligned} \max_{\Delta^{SC}} \left\| \mathbf{P}_{\tilde{\mathbf{T}}_{ext} \rightarrow \tilde{\Theta}_{APE}^{SC}} (s, \Delta^{SC}, \Pi^{SC}, \mathbf{K}_{ACS}) \right\|_{\infty} &\leq 1 \quad \text{(Req1)} \\ \max_{\Delta^{SC}} \left\| \mathbf{P}_{\tilde{\mathbf{T}}_{ext} \rightarrow \tilde{\Theta}_{RPE}^{SC}} (s, \Delta^{SC}, \Pi^{SC}, \mathbf{K}_{ACS}) \right\|_{\infty} &\leq 1 \quad \text{(Req2)} \\ \max_{\Delta^{SC}} \left\| \mathbf{P}_{\tilde{\mathbf{T}}_{ext} \rightarrow \tilde{\mathbf{u}}} (s, \Delta^{SC}, \Pi^{SC}, \mathbf{K}_{ACS}) \right\|_{\infty} &\leq 1 \quad \text{(Req3)} \\ \max_{\Delta^{SC}} \left\| \mathbf{P}_{\tilde{\mathbf{T}}_{ext} \rightarrow \tilde{\mathbf{T}}} (s, \Delta^{SC}, \Pi^{SC}, \mathbf{K}_{ACS}) \right\|_{\infty} &\leq 1 \quad \text{(Req4)} \end{aligned} \tag{17}$$

### 4 Optimization methods

In this section the *distributed* and *monolithic* optimization algorithms used in this study are detailed.

#### 4.1 Distributed architecture

In a *distributed* optimization architecture, a global optimization algorithm generates at each iteration  $i$  a set of  $N_s$  sub-iterations and corresponding  $N_s$  vectors of structural optimization parameters  $\chi^{i,s}$ , with  $s = 1, \dots, N_s$ . At each sub-iteration  $s$ , a nested control optimization is solved as shown in Eq. (2), where here  $\mathbf{y}_s = \chi^{i,s}$ . The population  $\chi^{i+1,s}$  (with  $s = 1, \dots, N_s$ ) of the next iteration is then chosen in the imposed ranges  $\mathbf{r}_\chi$  of each optimization parameter with a ratio based on the evaluation of the  $N_s$  objective functions  $J^s$  obtained at the previous iteration. The global optimization algorithm finally provides the best

particle  $\hat{\chi}$  after some stopping criteria are reached. In this study the chosen global optimization algorithm is the Particle Swarm Optimization (PSO) (Kennedy and Eberhart 1995), implemented in the MATLAB Global Optimization Toolbox. The full *distributed* optimization routine proposed in this study is synthesized in Algorithm 1. Note that for each sub-iteration a child BDF NASTRAN file (BDF\_C) is written from a parent one (BDF\_P) for each flexible sub-structure  $\mathcal{A}_j$ . NASTRAN is then called from MATLAB to analyse the sub-structure and produce the corresponding f06 result file, that is then used in SDTlib to build the corresponding TITOP model  $[\mathcal{M}_{\mathcal{A}_j}^{A_j}]_{\mathcal{R}_{\mathcal{A}_j}} (s, \Delta_{\mathcal{A}_j})$ . Before proceeding with the nested optimization, a structural constraint has to be verified for the ENVISION benchmark. For structural safety of the solar panel in stowed configuration during the launch, the

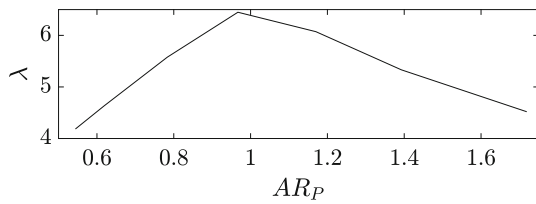


**Fig. 13** Launch constraint: computation of  $\lambda$  factor

following empirical hard constraint is introduced:

$$\omega_{STO} = \lambda \sqrt{\frac{R_P E_{Ph,sp}^3}{12\beta(1 - \nu_P)^2}} \quad [\text{rad/s}] \quad (18)$$

where  $R_P$  is the panel’s second moment of area,  $E_P$  is the skin Young’s Modulus,  $h_{sp}$  is the total honeycomb skin thickness and  $\nu_P$  is the Poisson’s ratio. Note that the expression to compute the second moment of area is;

$$R_P = \frac{12I_P}{h_{sp}^3} \quad (19)$$

where  $I_P = \left(\frac{t_{cp}}{2} + \frac{h_{sp}}{4}\right)^2$ . The parameter  $\beta$  is computed as:

$$\beta = \frac{\rho_s + \rho_c}{l_P w_P} \quad (20)$$

where  $\rho_s$  and  $\rho_c$  are respectively the mass per unit of area of the panel’s skin and the core,  $l_P$  is the length and  $w_P$  the width of each panel. Finally parameter  $\lambda$  is a function of the panel aspect ratio  $AR_P = l_P/w_P$  as shown in Fig. 13. To conclude,  $\omega_{STO}$  is a function of three optimization parameters ( $t_{sp}$ ,  $t_{cp}$  and  $AR_P$ ), the other ones being constant.

The constraint to be satisfied is then  $\omega_{STO} > \omega_L$ , where  $\omega_L = 76\pi$  rad/s. In case this test is not passed then a large value is assigned to the objective function of the current swarm sub-iteration:  $J^s = 10$ , in order to penalize the selection of this solution. If the launch constraint is satisfied, then the TITOP model of the entire spacecraft is computed with SDTlib and the nominal mass  $m$  can be recovered. With the structural optimization parameters fixed, a control optimization is now possible by solving problem (14) constrained by (15) with *syntune*. The global optimization optimization function of the current swarm sub-iteration can then be computed as:

$$J^s = \frac{m}{\bar{m}} + \sum_{j=1}^5 J_{c_j} \quad (21)$$

where  $\bar{m}$  is the maximum expected spacecraft overall mass, obtained by imposing the maximum value of each structural

parameter impacting the mass. Finally the PSO will terminate when a maximum number of iterations  $N_i$  is reached.

---

**Algorithm 1** Distributed Optimization

---

```

Inputs:  $\mathbf{r}_\chi$ , BDF_P,  $\omega_L$ ,  $N_i$ ,  $N_s$ ,  $\Delta^{SC}$ 
1: Initialize  $i, \hat{J}$ 
2: while  $i \neq N_i$  do
3:   Create  $\chi^{i,s}$ , with  $s = 1, \dots, N_s$ 
4:   for each  $s$  do
5:     for each flexible structure  $\mathcal{A}_j$  do
6:       Create BDF_C
7:       Run NASTRAN analysis with  $\chi^{i,s}$ 
8:       Compute  $[\mathcal{M}_{\mathcal{A}_j}^{A_j}]_{\mathcal{R}_{\mathcal{A}_j}}(s, \Delta_{\mathcal{A}_j})$ 
9:     end for
10:    Compute  $\omega_{STO}^s$ 
11:    if  $\omega_{STO}^s \leq \omega_L$  then
12:       $J^s \leftarrow 10$ 
13:    else if  $\omega_{STO}^s > \omega_L$  then
14:      Compute  $[\mathcal{M}_B^{SC}]_{\mathcal{R}_B}^{-1}(s, \Delta^{SC})$ 
15:       $m \leftarrow [\mathcal{M}_B^{SC}]_{\mathcal{R}_B}^{-1} \mathbf{w}_{\text{ext}/B,B(1) \rightarrow \ddot{x}_B(1)}(0)$ 
16:      Initialize  $\mathbf{K}_{ACS}$ 
17:      Solve (14) subject to (15)
18:       $J^s \leftarrow \frac{m}{\bar{m}} + \sum_{j=1}^5 J_{c_j}$ 
19:      if  $J^s < \hat{J}$  then
20:         $\hat{J} \leftarrow J^s$ 
21:         $\hat{\chi} \leftarrow \chi^{i,s}$ 
22:         $\hat{\mathbf{K}}_{ACS} \leftarrow \mathbf{K}_{ACS}$ 
23:      end if
24:    end if
25:     $i \leftarrow i + 1$ 
26:  end for
27: end while
28: return  $\hat{\chi}, \hat{\mathbf{K}}_{ACS}$ 

```

---

▷ See Eq. (11)

**4.2 Monolithic architecture**

In the *monolithic* optimization architecture, the control optimization routine handles the structure optimization as well as already shown in Sect. 3. Algorithm 2 lists the main steps.

---

**Algorithm 2** Monolithic Optimization

---

```

Inputs:  $\mathbf{r}_\chi$ ,  $\Delta^{SC}$ 
1: Initialize  $\Pi^{SC}$ 
2: Compute  $[\mathcal{M}_B^{SC}]_{\mathcal{R}_B}^{-1}(s, \Delta^{SC}, \Pi^{SC})$ 
3: Initialize  $\mathbf{K}_{ACS}$ 
4: Solve (16) subject to (17)
5: Compute  $\hat{\chi}$  from  $\hat{\Pi}^{SC}$ 
6: return  $\hat{\chi}, \hat{\mathbf{K}}_{ACS}$ 

```

---

▷ See Section 2.2.2

▷ See Eq. (11)

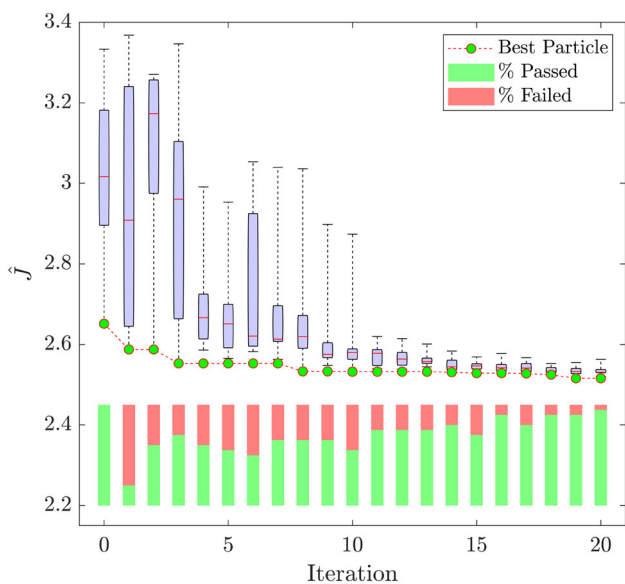


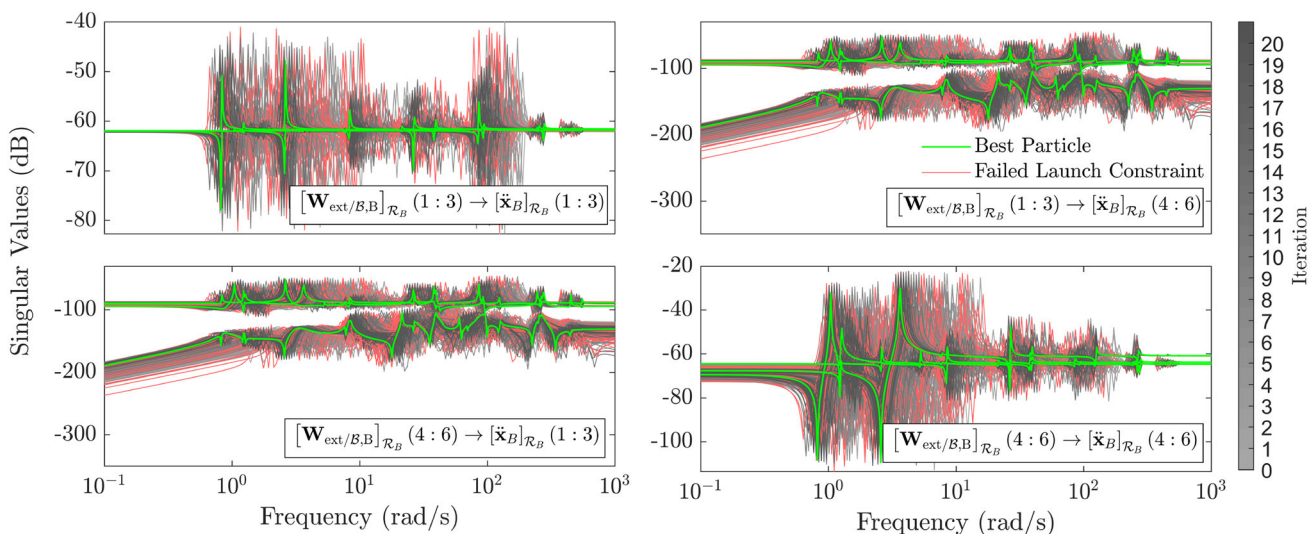
**Fig. 14** Evolution of the objective function along the PSO iterations. (Color figure online)

### 5 Results

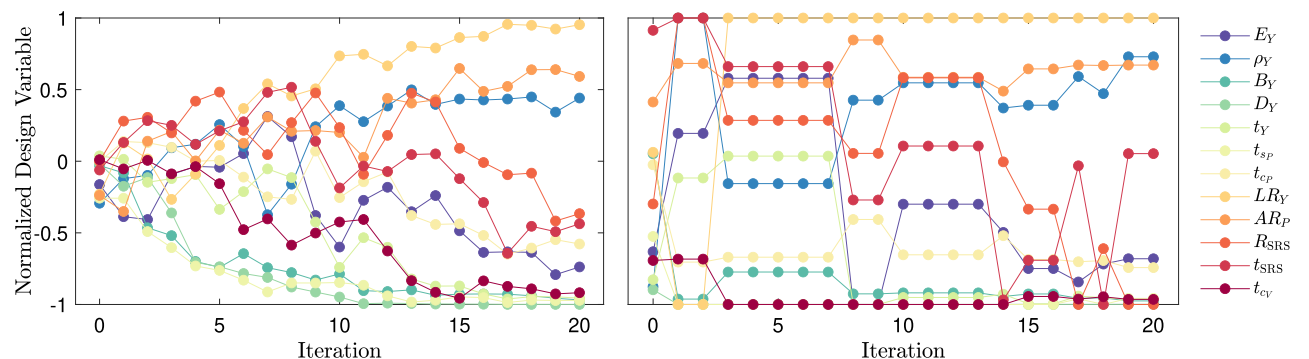
For the *distributed* optimization of the ENVISION benchmark the 12 structural optimization parameters in Table 2 are considered. After a trial and error process the maximum number of PSO iterations and sub-iterations have been fixed to  $N_i = 20$  and  $N_s = 20$  respectively as compromise between computational time and convergence to the optimal solution. Figure 14 shows the evolution of the objective function  $\hat{J}$  along the iterations, with quantiles (blue boxes) of the swarm particles having passed the launch constraint test. The dispersion of the particles reduces along the iterations by giving an indication on the convergence to the optimal solution.

Figure 15 shows the evolution of the singular values for all particle swarm iterations. Notice as the optimal solution attracts all modes' resonances to lower frequencies by making the spacecraft lighter and more flexible.

A detail of the evolution of each optimization parameter is provided in Fig. 16.



**Fig. 15** Singular values of all swarm particles along the optimization iterations



**Fig. 16** Evolution of the optimal structure parameters along the PSO iterations: average value among particle swarms of the same iteration (left) and best particle (right)

**Table 3** General performance of *distributed* and *monolithic* optimization

	Distributed	Monolithic
Opt. total time (h)	12.33	0.4072
Opt. SC total mass (kg)	1253.86	1258.166
Total mass reduction (kg)	55.94	51.63
% opt. total mass	4.27%	3.94%
Opt. max control perf	0.7208	1.0011

**Table 4** Optimized control performance with *distributed* and *monolithic* optimization

Cont. req.	Distributed	Monolithic
APE	0.7208 ( $\bar{\mu}_\Delta = 0.7353$ )	1.0011 ( $\bar{\mu}_\Delta = 1.00051$ )
RPE	0.0583	0.1016
Command	0.0122	0.0157
Sensitivity	0.7208 ( $\bar{\mu}_\Delta = 0.7530$ )	1.0011 ( $\bar{\mu}_\Delta = 1.01$ )
Noise variance	0.0469	0.0521

For the *monolithic* optimization, four optimization parameters are chosen ( $t_{sp}$ ,  $t_{cp}$ ,  $R_{SRS}$  and  $t_{cv}$ ) as already mentioned in Sect. 2.2.2. All the other parameters are fixed to their mean value in order to respect the launch constraint. This constraint cannot in fact easily be included in the *monolithic* approach as in the *distributed* one.

The optimal mechanical parameters obtained with both *distributed* and *monolithic* optimization are shown in Table 2. We notice as parameters mostly impacting the mass (Fig. 16) tend to reach their minimum value except for the SAR core thickness, that surprisingly reaches its maximum value in the *monolithic* optimization. This result can be interpreted with the fact that the *monolithic* optimization is based on a non-smooth gradient based optimization, that could fall into a local minimum. However, the advantage of using a *monolithic* optimization is the needed computational time with respect to the *distributed* architecture as shown in Table 3. The optimization total time for the *distributed* architecture is 12.33 h versus  $\approx 0.4$  h needed for the *monolithic* one. It has to be said that for the *monolithic* architecture a previous initialization of  $\Pi^{SC}$  (step 1 in Algorithm 2) is not here taken into account. This time depends on the number of NAS-TRAN analyses to be run to have the initial set of samples to be interpolated with APRICOT. This operation is generally really fast and for the present application stayed smaller than  $\approx 0.5$  hours. Finally, the APRICOT generation of  $\Pi^{SC}$  took just 6.335 s. Notice that both optimizations have been run on a Windows 7, 64 bits, Intel(R) Core(TM) i7-4810MQ CPU @ 2.80GHz, RAM 16 Go. The huge difference in the optimization time between *monolithic* and *distributed* architecture is due to the robust control synthesis step. Even if in

**Table 5** Optimal control parameters obtained with *distributed* and *monolithic* optimization

	Distributed	Monolithic
$K_p^x$	35.0764 (8.6952)	35.2731 (8.8499)
$K_v^x$	335.2577 (202.8248)	201.3181 (206.4978)
$K_p^y$	13.9779 (6.1029)	14.8800 (6.2416)
$K_v^y$	280.8861 (142.4001)	162.0921 (145.6371)
$K_p^z$	35.008 (10.5454)	35.2562 (10.7226)
$K_v^z$	404.4305 (246.0605)	227.9570 (250.1946)

Values in brackets are the initial guess obtained with Eq. (11)

the *monolithic* architecture the set of considered uncertainties is bigger (to take into account the optimization parameters in  $\Pi^{SC}$ ) than in the *distributed* architecture, the synthesis is run ones. In the *distributed* architecture, a new control synthesis is conversely run at each swarm iteration. Even if the achieved optimized mass is similar with the two approaches, if with a *distributed* architecture a big number of optimization parameters can be considered (with a consequent lower computational time), with the *monolithic* optimization a small set of mechanical parameters can be used. This number is in fact limited as seen in the previous sections by the complexity of the interpolated LFT, that can contain a huge number of uncertain repeated parameters, which can make the robust control optimization infeasible. In this study four parameters out of twelve have been chosen based on their impact on the overall spacecraft mass. This choice on the other hand constrains the achievable control performance, that is driven by other parameters as discussed in Sect. 5.1.

As shown in Table 3, the achieved mass reduction is almost the same with the two approaches. Notice that the nominal mass of the central body corresponds to 1173 kg, that means that the actual percentage of saved mass with respect to the potential reducible mass (of the flexible appendages) corresponds indeed to 69.18% and 63.85%, for the *distributed* and *monolithic* optimization respectively. Concerning the control performance with the *distributed* architecture, the maximum control index ( $\max_j J_{c_j} = 0.7208 < 1$  with  $j = 1, \dots, 5$ ) shows that control performance is largely satisfied. For *monolithic* architecture, this index is slightly greater than unity, while acceptable by keeping in mind that a large uncertainty level has been considered (see Table 1). Details regarding each achieved control index are provided in Table 4. From this table, the APE and Sensitivity indexes result to be the most critical to be satisfied.

Table 5 finally provides the optimal control gains obtained with both optimization approaches.

A deeper analysis is proposed in Sect. 5.1 to better interpret physically the achieved results by using the outcomes of the *distributed* optimization.



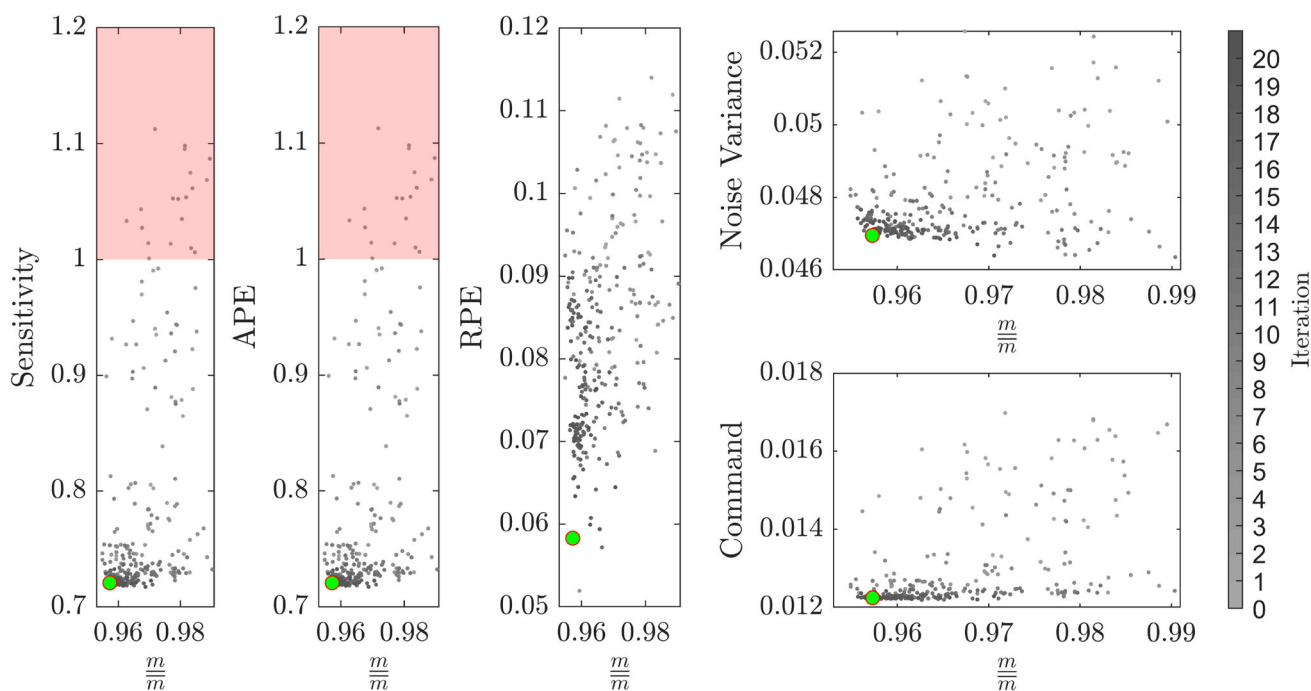


**Fig. 17** Pareto fronts for the *distributed* optimization: control versus structure performance indexes. The green bullet represents the best particle. (Color figure online)

### 5.1 Further analysis with *distributed* optimization

The concurrent character of the proposed structure/control optimization is shown in the Pareto fronts of Fig. 17. An excessive reduction of the spacecraft mass (with all structural parameters converging to their minimum values) corresponds both to a degradation of the pointing performance (APE channel) and stability (Sensitivity channel). The optimal solution (green bullet) represents the compromise between these competing objectives. In particular an excessive reduction of the Yoke length ratio  $LR_Y$  corresponds to a loss of the spacecraft stability. This point is further discussed in the following paragraphs.

The impact of each structural optimization parameter on both structural and control optimization indexes can be highlighted by plotting the evolution of the particle swarms along the PSO iterations as done in Figs. 18 and 19 respectively. The linear dispersion of particles according to a variation of  $t_{cp}$  confirms the importance of this parameter for a reduction of the spacecraft mass. A similar behavior, while less marked, can be noticed for  $t_{sp}$  and  $t_{cv}$ , as expected. Another observation is that a square-like configuration of the solar panels is preferred to a rectangular one since particles with extreme values of  $AR_P$  are discarded since the launch constraint is not satisfied.

According to control performance, Fig. 19 reveals the key structural parameters having the most important impact. As already shown in Table 4, APE and Sensitivity indexes are

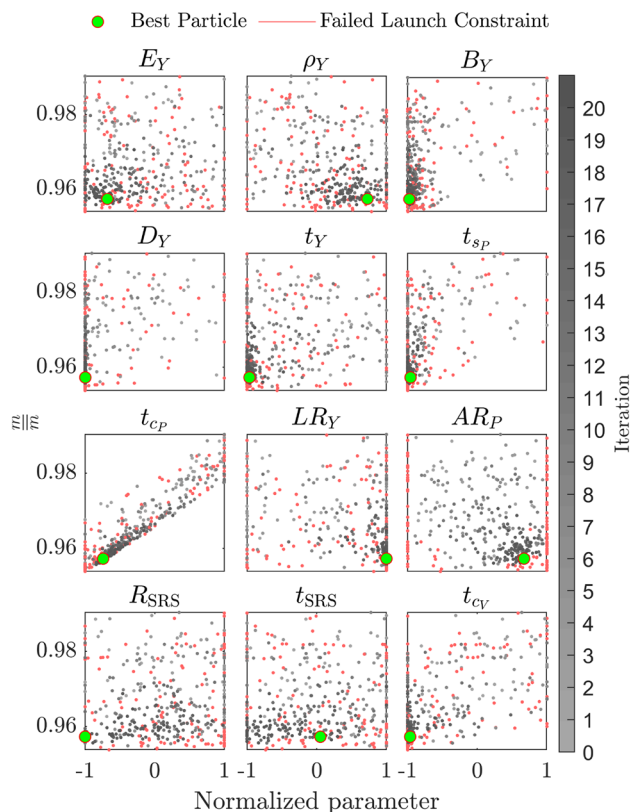


**Fig. 18** Mass optimization cost function versus structure optimization parameters

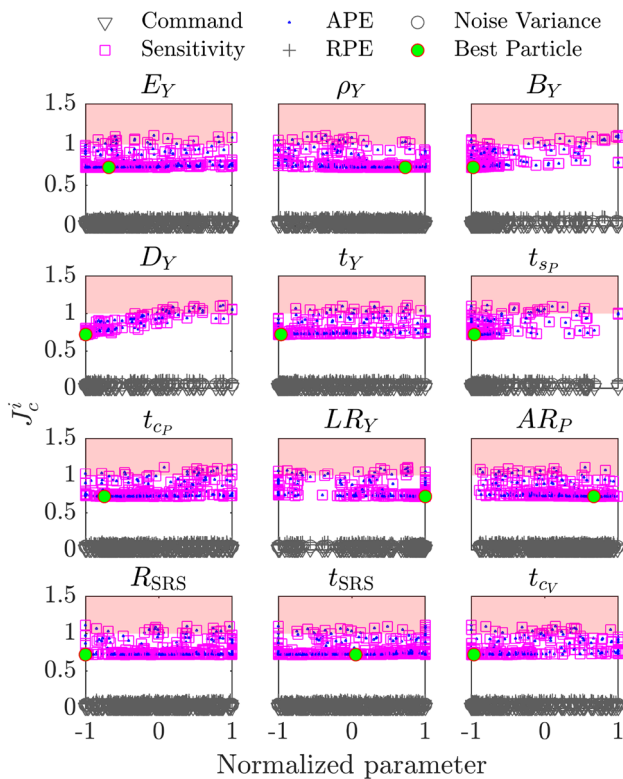


**Fig. 19** Control optimization cost function versus structure optimization parameters

the ones driving the overall control performance. They get the same value in the vast majority of cases according to the gradient-based algorithm implemented in the *systeme* routine. By looking at the dispersion of particles along the iterations, a clear dependence (linear) of control performance is noticed when Yoke’s section dimensions (mostly  $B_Y$  and  $D_Y$ ) vary. In particular a degradation is experienced when bigger values of  $B_Y$  and  $D_Y$  are used.

In order to better analyze this impact on the control performance, a further analysis is performed: worst-case (WC) APE and Sensitivity performance are checked when one optimization parameter is left varying by keeping all the others equal to the values corresponding to the optimal solution. In order to speed up the computation, a formal  $\mu$ -analysis is not applied for this analysis and *systeme* is used to obtain the worst-case peak gain of the demanded transfer functions (APE and Sensitivity channels). The research of the worst-case configuration in *systeme* is in fact based on a heuristic search and not a  $\mu$ -based one (see Apkarian et al. (2015) for more details). For this reason a formal validation of the synthesized controller through a  $\mu$ -analysis is proposed in Sect. 5.2. Since here the objective is to show the overall trend of the control performance with a variation of the structural parameters around the optimal configuration, an estimation of the WC is sufficient. The WC analysis is then turned into

a parametric robust control design problem: the upper bound  $\bar{p}_{WC}$  of the peak gain  $p_{WC}$  of the analyzed transfer function is considered as a decision variable and the objective is to minimize  $\bar{p}_{WC}$  whilst meeting the constraint:

$$\max_{\Delta^{SC} \in \mathcal{D}_{\Delta^{SC}}} \left\| \frac{\mathbf{H}(s, \Delta^{SC})}{\bar{p}_{WC}} \right\|_{\infty} \leq 1 \tag{22}$$

where  $\mathbf{H}(s, \Delta^{SC})$  is the transfer function to be checked and  $\mathcal{D}_{\Delta^{SC}}$  is a subset of the parametric domain in which the parametric uncertainties  $\Delta^{SC}$  can vary. This subset is chosen by *systeme* as said before. By running this analysis, the results are provided in Fig. 20. A first observation is that a variation of all parameters around the optimal solution does not critically affect the APE performance since the WC stays below unity. However, a degradation of the pointing performance is experienced with growing values of  $t_{cp}$ ,  $t_{sp}$ ,  $LR_Y$  and  $AR_P$ . More critical is the impact of a variation of the parameters on the spacecraft stability (Sensitivity channel). An increase of one of the dimension of the Yoke’s section ( $D_Y$ ) around the optimal solution corresponds in fact to a fast degradation of the stability margins. This phenomenon is better highlighted in Fig. 21, where the singular values of the worst-case Sensitivity channel are plotted with a variation of  $D_Y$  around the optimal solution. An amplification of a flexible mode is experienced with growing values of  $D_Y$  and a maximum loss of  $\approx 20\%$  of stability performance is reached. This analysis explains also the worst control performance obtained with the *monolithic* approach since an average values is chosen for  $D_Y$ .

In Fig. 20 it is also interesting to notice that a reduction of the Yoke length ratio  $LR_Y$  corresponds to a degradation of the spacecraft stability. This phenomenon explains the Pareto front behavior discussed at the beginning of this section.

### 5.2 Controller formal validation

In order to certify the synthesized controllers both for *distributed* and *monolithic* optimization it is necessary to rigorously validate the worst-case control performance. As already mentioned, *systeme* routine is based on a heuristic search of the worst-case configurations. Formal validation with the computation of the structured singular value  $\mu_{\Delta}$  is thus needed (Zhou and Doyle 1998). The uncertain parameter  $\sigma_4$  related to the solar panel geometrical configuration is repeated 32 times in the uncertain block  $\Delta^{SC}$  by leading to unacceptable computational time using the standard worst-case analysis tools. This problem is circumvented by sampling  $\sigma_4$  on a grid of  $N_{\tau} = 50$  points regularly *distributed* in  $[0, 1]$ . This subset has been chosen to account for the symmetric configuration of the model in the  $\theta_{SA} \in [0, 180]^{\circ}$  and  $\theta_{SA} \in [-180, 0]^{\circ}$  intervals.

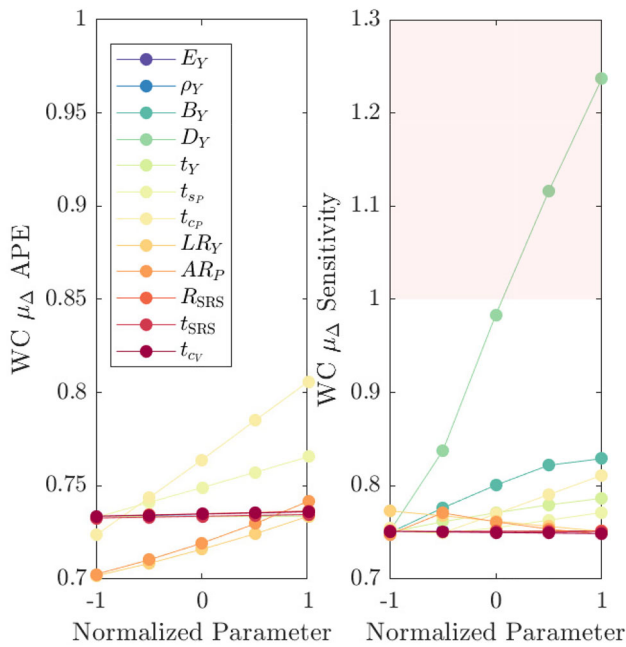


**Fig. 20** Sensitivity of the worst-case peak gain for APE and Sensitivity channel around the optimal solution

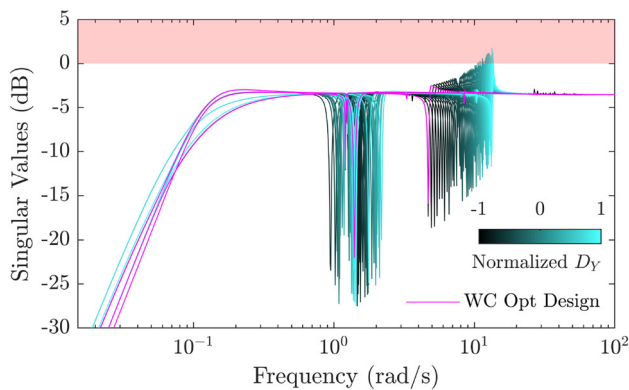


**Fig. 21** Estimation of WC Sensitivity control performance with variation of  $D_Y$  in the optimal *distributed* design

The computation of  $\mu_\Delta$  lower and upper bounds is performed thanks to the *wcgain* routine in MATLAB Robust Control Toolbox. The worst-case parametric configuration is associated to the lower bound  $\underline{\mu}_\Delta$ . The upper bound  $\bar{\mu}_\Delta$  computation provides the conservatism in the estimation of the true value of  $\mu_\Delta$ . Note that this analysis is only performed for the two most critical control performance, the APE and Sensitivity (see Table 4):

$$\begin{aligned} \mu_\Delta^{\text{APE}} &= \max_{\Delta^{SC}} \left\| \mathbf{P}_{\tilde{\mathbf{T}}_{\text{ext}} \rightarrow \tilde{\Theta}_{\text{APE}}^{SC}}(s, \Delta^{SC}, \mathbf{K}_{\text{ACS}}) \right\|_\infty \\ \mu_\Delta^{\text{Sensitivity}} &= \max_{\Delta^{SC}} \left\| \mathbf{P}_{\tilde{\mathbf{T}}_{\text{ext}} \rightarrow \tilde{\mathbf{T}}}(s, \Delta^{SC}, \mathbf{K}_{\text{ACS}}) \right\|_\infty \end{aligned} \quad (23)$$

Figures 22 and 23 show the results of this analysis for the *distributed* and *monolithic* architectures respectively. Note that for this validation the optimal parameters obtained with the *monolithic* approach are used to generate a new dynamical model directly with NASTRAN in order to avoid the use of the model based on the fitted block  $\Pi^{SC}$ .

One can check that the gaps between the upper and the lower bounds of  $\mu_\Delta$  are tight by showing that the WC performance is accurately evaluated and very close to the value provided by *systeme*. In the same figure the WC combination of parameters corresponding to the overall worst-case  $\mu_\Delta$  is provided as well. For both optimization architectures, the largest degradation is obtained for the minimal value of the central body inertia, that can be physically explained with a consequent bigger contribution of the flexible structural parts to the spacecraft dynamics.

### 5.3 Lesson learned

This section is intended to provide some feedback on the practical use of the two optimization architectures proposed in this work. When a fast solution is needed and the set of design parameters can be reduced to few, a *monolithic* architecture has to be preferred. This is especially valid for missions where the control problem is not extremely challenging, as in the proposed benchmark. However, when pointing requirements become tighter as for telescope Science missions, a greater number of degrees of freedom would offer more flexibility to reach the expected level of performance. For a similar mass reduction, with the *distributed* architecture, almost 30% was gained on the control performance of the ENVISION benchmark with respect to the *monolithic* optimization. Moreover, the *distributed* architecture allows the integration of a larger type of structural constraints than the *monolithic* one, by keeping a direct connection with the FEM solver. Structural constraints, like maximum strength tolerated by the structure, can easily be included as it was shown in this paper with the launch constraint. The price to pay is nevertheless an increase in the computational time. This computational cost could benefit of parallel computing, for which Algorithm 1 is easily adaptable.

## 6 Conclusion

In this work, an end-to-end methodology was presented for robust design of structure/control co-optimization problems. Both a *distributed* and a *monolithic* optimization architectures were proposed and applied to a scientific ESA spacecraft benchmark. It was shown how the TITOP modeling approach is well suited to take into account all parametric uncertainties and optimization variable in a unique LFT

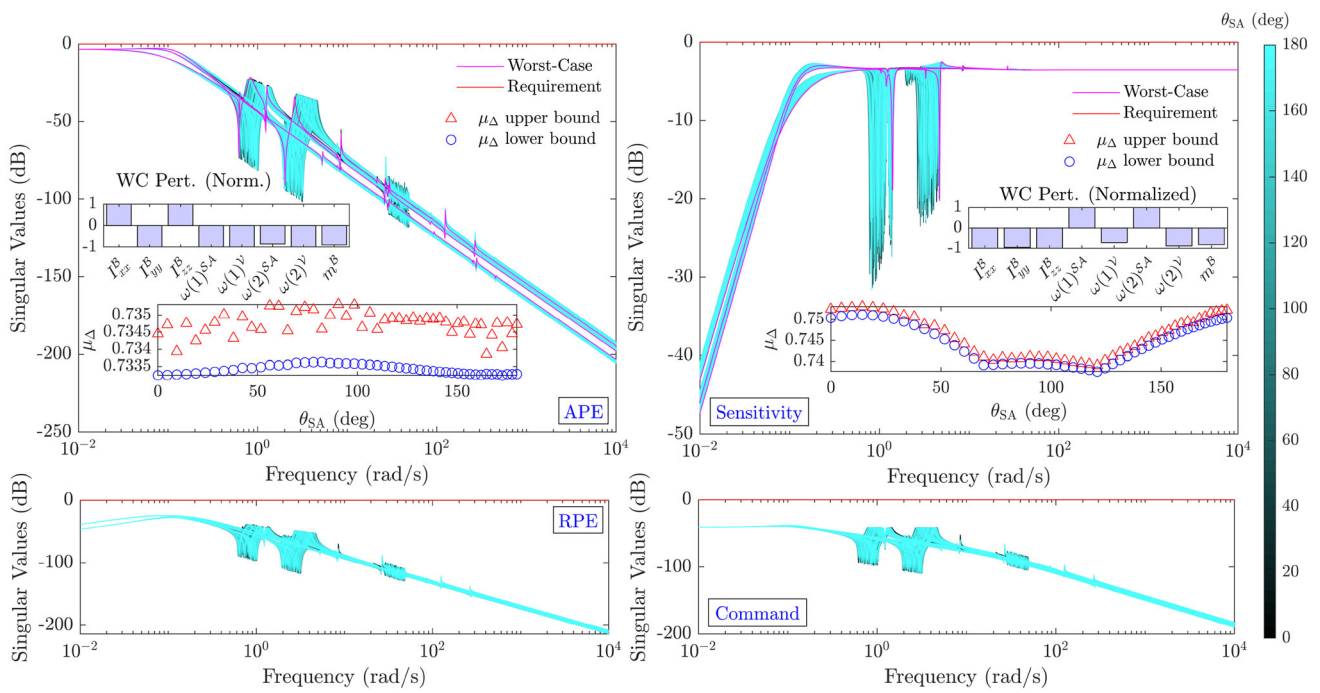


Fig. 22 Worst-case analysis of control performance for *distributed* optimization

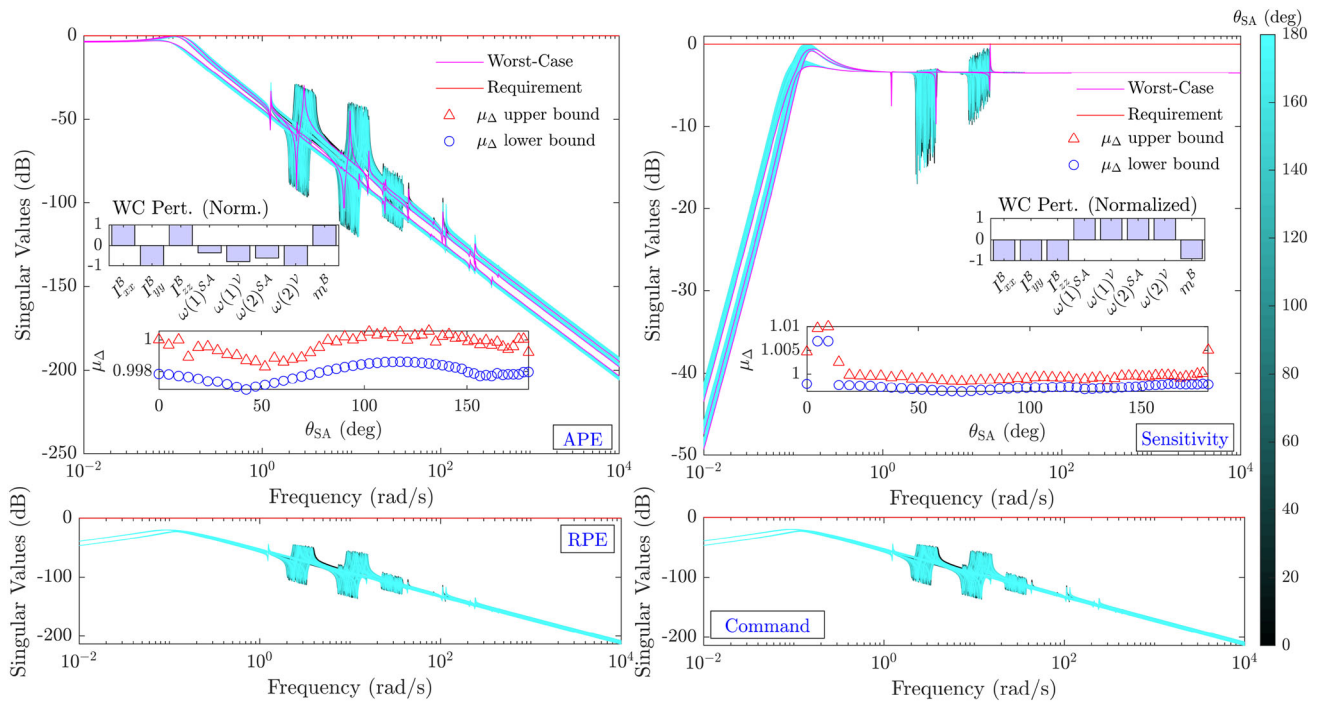


Fig. 23 Worst-case analysis of control performance for *monolithic* optimization

model, that can be used to obtain a robust optimal solution in a straightforward way. Moreover, the LFT framework is useful for final validation of the achieved control performances. With both the *distributed* and *monolithic* architecture an important reduction of the spacecraft mass is achieved by meeting the mission control performance. This point demonstrated the importance of treating the problem of structure and control optimization in the same framework and avoid the sequential approach traditionally employed in the industrial context. The methodology proposed in this paper contributes in fact to reduce the design iterations between the structure and control departments and enhance the optimization performance. The gain in the efficiency of the design process benefits of the LFT formalism as well. Inclusion of uncertainties in the modeling step allows to directly obtain robust control solutions by limiting the tuning iterations to satisfy all critical configurations and speed up the validation process by formally detecting possible worst-case with the help of  $\mu$ -analysis. The limits of both optimization architectures was also discussed: when using a *distributed* architecture a longer computational time is the price to pay for including a bigger set of optimization parameters with respect to the *monolithic* architecture. The LFT complexity drives in fact the maximum number of optimization variables in the *monolithic* approach. As seen for the ENVISION benchmark, this parameters' selection brought, as compromise, to a worse control performance, by reaching the same mass reduction as for the *distributed* optimization. It was also shown that, with the *distributed* approach, it is possible to introduce exogenous structural constraints (like the launch constraint in this work), which relies on further structural analysis at each iteration. The *distributed* approach also makes a deeper physical understanding of the achieved results possible by giving access to the evolution of the structural parameters during the optimization iterations.

**Funding** This work was supported by the European Space Agency (ESA) (Contract No. 4000133632/21/NL/CRS) in the context of the Open Invitations To Tender (ITT) "Control/structure codesign for planetary spacecraft with large flexible appendages" (AO/1-10332/20/NL/CRS).

## Declarations

**Conflict of interest** On behalf of all authors, the corresponding author states that there is no conflict of interest.

**Replication of results** Upon reasonable request the authors are willing to share part of the MATLAB code used to generate the results in this paper. Industrial data are not available.

## References

- Alavi A, Dolatabadi M, Mashhadi J, Noroozinejad Farsangi E (2021) Simultaneous optimization approach for combined control-structural design versus the conventional sequential optimization method. *Struct Multidisc Optim* 63:1367–1383
- Alazard D, Finozzi A, Sanfedino F (2023) Port inversions of parametric two-input two-output port models of flexible substructures. *Multibody Syst Dyn* 57(3–4):365–387
- Alazard D, Loquen T, De Plinval H, Cumer C (2013) Avionics/control co-design for large flexible space structures. In: AIAA Guidance, Navigation, and Control (GNC) conference, p 4638
- Alazard D, Perez JA, Cumer C, Loquen T (2015) Two-input two-output port model for mechanical systems. In: AIAA Guidance, Navigation, and Control conference, p 1778
- Alazard D, Sanfedino F (2020) Satellite dynamics toolbox for preliminary design phase. In: 43rd Annual AAS Guidance and Control conference, vol 30, pp 1461–1472
- Allison JT, Guo T, Han Z (2014) Co-design of an active suspension using simultaneous dynamic optimization. *J Mech Des* 136(8):081003
- Apkarian P, Bompard V, Noll D (2007) Non-smooth structured control design with application to PID loop-shaping of a process. *Int J Robust Nonlinear Control* 17(14):1320–1342. <https://doi.org/10.1002/rnc.1175>
- Apkarian P, Dao MN, Noll D (2015) Parametric robust structured control design. *IEEE Trans Automatic Control* 60(7):1857–1869
- Azad S, Herber DR (2023) An overview of uncertain control co-design formulations. *J Mech Des* 145(9):091709. <https://doi.org/10.1115/1.4062753>
- Chebbi J, Dubanchet V, Gonzalez JAP, Alazard D (2017) Linear dynamics of flexible multibody systems. *Multibody Syst Dyn*. <https://doi.org/10.1007/s11044-016-9559-y>
- Chen CY, Cheng CC (2006) 3d model based design for control of a mechatronic machine tools system. *Mater Sci Forum Prog Adv Manuf Micro/Nano Technol* 505–507:967–972
- Chilan CM, Herber DR, Nakka YK, Chung S-J, Allison JT, Aldrich JB, Alvarez-Salazar OS (2017) Co-design of strain-actuated solar arrays for spacecraft precision pointing and jitter reduction. *AIAA J* 55(9):3180–3195
- Dubanchet V (2016) Modeling and control of a flexible space robot to capture a tumbling debris. PhD Thesis, Ecole Polytechnique, Montreal (Canada)
- Falcoz A, Watt M, Yu M, Kron A, Menon PP, Bates D, Massotti L (2013) Integrated control and structure design framework for spacecraft applied to biomass satellite. In: IFAC proceedings volumes (19th IFAC symposium on automatic control in aerospace), vol 46(19), pp 13–18
- Fathy H, Reyer J, Papalambros P, Ulsov A (2001) On the coupling between the plant and controller optimization problems. In: Proceedings of the 2001 American control conference, vol 3, pp 1864–1869
- Feng Z, Zhang Q, Tang Q, Yang T, Ge J (2014) Control-structure integrated multi-objective design for flexible spacecraft using MOEA/D. *Struct Multidisc Optim* 50:347–362
- Frischknecht BD, Peters DL, Papalambros PY (2011) Pareto set analysis: local measures of objective coupling in multiobjective design optimization. *Struct Multidisc Optim* 43(5):617–630
- Gahinet P, Apkarian P (2011) Structured  $\mathcal{H}_\infty$  synthesis in Matlab. In: IFAC proceedings volumes (18th IFAC World Congress), vol 44(1), pp 1435–1440
- He H, Li Y, Clare L, Jiang JZ, Al Sakka M, Dhaens M, Conn A (2023) A configuration-optimisation method for passive-active-combined suspension design. *Int J Mech Sci* 258:108560. <https://doi.org/10.1016/j.ijmecsci.2023.108560>

- Herber DR, Allison JT (2018) Nested and simultaneous solution strategies for general combined plant and control design problems. *J Mech Des* 141(1):011402. <https://doi.org/10.1115/1.4040705>
- Kennedy J, Eberhart R (1995) Particle swarm optimization. In: Proceedings of ICCNN'95—international conference on neural networks, vol 4, pp 1942–1948. <https://doi.org/10.1109/ICNN.1995.488968>
- Li Q, Zhang W, Chen L (2001) Design for control—a concurrent engineering approach for mechatronic systems design. *IEEE/ASME Trans Mechatron* 6(2):161–169
- Maraniello S, Palacios R (2016) Optimal vibration control and co-design of very flexible actuated structures. *J Sound Vib* 377:1–21
- Martins JR, Lambe AB (2013) Multidisciplinary design optimization: a survey of architectures. *AIAA J* 51(9):2049–2075
- Perez JA, Pittet C, Alazard D, Loquen T, Cumer C (2015) A flexible appendage model for use in integrated control/ structure spacecraft design. In: 1st IFAC workshop on advanced control and navigation for autonomous aerospace vehicles (ACNAAV'15) (IFAC Papers Online), vol 48(9), pp 275–280
- Poussot-Vassal C, Roos C (2012) Generation of a reduced-order LPV/LFT model from a set of large-scale MIMO LTI flexible aircraft models. *Control Eng Pract* 20(9):919–930
- Reyer JA, Fathy HK, Papalambros PY, Ulsoy AG (2001) Comparison of combined embodiment design and control optimization strategies using optimality conditions. In: 27th International design engineering technical conferences and computers and information in engineering conference, pp 1023–1032
- Roos C, Hardier G, Biannic J-M (2014) Polynomial and rational approximation with the apricot library of the SMAC toolbox. In: 2014 IEEE conference on control applications (CCA), pp 1473–1478
- Sanfedino F (2019) Experimental validation of a high accuracy pointing system. PhD Thesis, ISAE-SUPAERO, Toulouse
- Sanfedino F, Alazard D, Pommier-Budinger V, Falcoz A, Boquet F (2018) Finite element based n-port model for preliminary design of multibody systems. *J Sound Vib* 415:128–146
- Sanfedino F, Alazard D, Preda V, Oddenino D (2022) Integrated modeling of microvibrations induced by solar array drive mechanism for worst-case end-to-end analysis and robust disturbance estimation. *Mech Syst Signal Process* 163:108168
- Toglia C, Pavia P, Campolo G, Alazard D, Loquen T, de Plinval H, Massotti L (2013) Optimal co-design for Earth observation satellites with flexible appendages. In: AIAA Guidance, Navigation, and Control (GNC) conference, p 4640
- Zhao G, Chen B, Gu Y (2009) Control-structural design optimization for vibration of piezoelectric intelligent truss structures. *Struct Multidisc Optim* 37:509–519
- Zheng H, Zhang S, Zhao G (2021) Integrated design optimization of actuator layout and structural ply parameters for the dynamic shape control of piezoelectric laminated curved shell structures. *Struct Multidisc Optim* 63:2375–2398
- Zhou K, Doyle JC (1998) *Essentials of robust control*. Prentice-Hall, Upper Saddle River

**Publisher's Note** Springer Nature remains neutral with regard to jurisdictional claims in published maps and institutional affiliations.

Springer Nature or its licensor (e.g. a society or other partner) holds exclusive rights to this article under a publishing agreement with the author(s) or other rightsholder(s); author self-archiving of the accepted manuscript version of this article is solely governed by the terms of such publishing agreement and applicable law.